

# Level structure of light neutron-rich La isotopes beyond the N=82 shell closure

A. Navin,<sup>1,\*</sup> E. H. Wang,<sup>2,3,4,\*</sup> S. Bhattacharyya,<sup>5,6</sup> Menglan Liu,<sup>7</sup> Cenxi Yuan,<sup>7</sup> M. Rejmund,<sup>1</sup> A. Lemasson,<sup>1</sup> S. Biswas,<sup>1,†</sup> Y.H. Kim,<sup>8,‡</sup> C. Michelagnoli,<sup>1,§</sup> J. H. Hamilton,<sup>4</sup> A. V. Ramayya,<sup>4</sup> I. Stefan,<sup>9</sup> R. Banik,<sup>5,¶</sup> P. Bednarczyk,<sup>10</sup> Soumik Bhattacharya,<sup>5</sup> E. Clément,<sup>1</sup> H.L. Crawford,<sup>11</sup> G. de France,<sup>1</sup> P. Fallon,<sup>11</sup> G. Frémont,<sup>1</sup> J. Goupil,<sup>1</sup> B. Jacquot,<sup>1</sup> H.J. Li,<sup>1</sup> J. Ljungvall,<sup>12,9</sup> Y. X. Luo,<sup>4,13</sup> A. Maj,<sup>10</sup> L. Ménager,<sup>1</sup> V. Morel,<sup>1</sup> G. Mukherjee,<sup>5,6</sup> R. Palit,<sup>14</sup> R.M. Pérez-Vidal,<sup>15</sup> J. O. Rasmussen,<sup>13</sup> J. Ropert,<sup>1</sup> C. Schmitt,<sup>1,\*\*\*</sup> and S. J. Zhu<sup>16</sup>

<sup>1</sup>GANIL, CEA/DRF-CNRS/IN2P3, Bd Henri Becquerel, BP 55027, F-14076 Caen Cedex 5, France

<sup>2</sup>Shandong Provincial Key Laboratory of Nuclear Science,  
Nuclear Energy Technology and Computer Utilization,

Weihai Frontier Innovation Institute of Nuclear Technology, School of Nuclear Science,  
Energy and Power Engineering, Shandong University, Jinan 250061, China.

<sup>3</sup>Weihai Research Institute of Industrial Technology of Shandong University, Weihai 264209, China

<sup>4</sup>Department of Physics and Astronomy, Vanderbilt University, Nashville, Tennessee 37235, USA

<sup>5</sup>Variable Energy Cyclotron Centre, 1/AF Bidhannagar, Kolkata 700064, India

<sup>6</sup>Homi Bhabha National Institute, Training School Complex, Anushaktinagar, Mumbai-400094, India

<sup>7</sup>Sino-French Institute of Nuclear Engineering and Technology, Sun Yat-sen University, Zhuhai 519082, China

<sup>8</sup>Center for Exotic Nuclear Studies, Institute for Basic Science, Daejeon 34126, Republic of Korea

<sup>9</sup>Université Paris-Saclay, CNRS/IN2P3, IJCLab, 91405 Orsay, France

<sup>10</sup>Institute of Nuclear Physics PAN, 31-342 Kraków, Poland

<sup>11</sup>Nuclear Science Division, Lawrence Berkeley National Laboratory, Berkeley, California 94720, USA

<sup>12</sup>Université de Strasbourg, CNRS, IPHC UMR 7178, 67000, Strasbourg, France

<sup>13</sup>Lawrence Berkeley National Laboratory, Berkeley, California 94720, USA

<sup>14</sup>Department of Nuclear and Atomic Physics, Tata Institute of Fundamental Research, Mumbai, 400005, India

<sup>15</sup>Instituto de Física Corpuscular, CSIC-Universitat de València, E-46980 València, Spain

<sup>16</sup>Department of Physics, Tsinghua University, Beijing 100084, People's Republic of China

(Dated: January 27, 2026)

The high spin excited states of Lanthanum isotopes  $^{140-143}\text{La}$ , above the  $N = 82$  closed shell, have been populated in fission reactions. The prompt  $\gamma$ -ray transitions were measured using two complementary methods; a) in coincidence with the isotopically identified fragments produced in the fission of the  $^{238}\text{U} + ^9\text{Be}$  system using the VAMOS++ and the AGATA spectrometers and b) high statistics three-fold  $\gamma - \gamma - \gamma$  and four-fold  $\gamma - \gamma - \gamma - \gamma$  coincidence data from the spontaneous fission of  $^{252}\text{Cf}$  using the Gammasphere. This work reports the first identification of a pair of parity doublet structures in  $^{143}\text{La}$  and the new high spin level structure in  $^{140-142}\text{La}$  from prompt  $\gamma$ -ray spectroscopy. The level structures are interpreted in terms of the systematics of neighbouring odd- $Z$  nuclei above  $Z = 50$  shell closure and large-scale shell model calculations. The present results indicate the presence of stable octupole deformation, in  $^{143}\text{La}$ . The excitation energy pattern and their comparison with neighbouring isotones, moving away from the  $N=82$  closed shell, point towards a transition from single particle structures to an alternating parity rotational band structure in the La isotopic chain.

## I. INTRODUCTION

Nuclei with few neutrons and protons above major shell closures are always of special interest as they provide important inputs regarding single particle configurations, neutron-proton interactions, shape evolution, etc.,

and also to improve the effective interaction for large scale shell model calculations. In particular, the odd- $A$  or odd-odd nuclei with respect to the even-even core are important because of the important role played by the odd valence particles in determining their level structure. As more and more valence protons are added to the  $Z = 50$  core, the nuclei begin to show a transition from near spherical to a deformed structure. Deformed nuclei can have both axial and reflection symmetry (prolate or oblate deformation), or can show reflection asymmetric shapes (manifested as octupole deformation) [1–3]. The existence of an "island of octupole collectivity" around  $Z = 56$  and  $N = 88$  is confirmed by extensive experimental observation of parity doublets in various isotopes in this region [4–16]. The nuclei in this region are suitable candidates to show octupole collectivity, as their Fermi levels lie between the  $f_{7/2}$  and  $i_{13/2}$  neutron orbitals and  $d_{5/2}$  and  $h_{11/2}$  proton orbitals, which differ by

\*Corresponding author

†Present address: Rutherford Appleton Laboratory, Fermi Ave, Harwell, Didcot OX11 0QX, United Kingdom

‡Present address: Center for Exotic Nuclear Studies, Institute for Basic Science, Daejeon 34126, Republic of Korea

§Present address: Institut Laue-Langevin, F-38042 Grenoble Cedex, France

¶Present address: Institute of Engineering and Management, Salt-lake Sector V, Kolkata 700091, India

\*\*\*Present address: IPHC Strasbourg, Université de Strasbourg-CNRS/IN2P3, F-67037 Strasbourg Cedex 2, France

$j = l = 3$  [17, 18]. Various experimental signatures to characterize stable octupole deformation include features of rotational bands [1, 2, 19]. The existence of parity doublet bands (pair of the states with spin  $I$  but of opposite parities and having strong interband E1 transitions) is one such signature. These bands are associated with the simplex quantum numbers  $s = \pm 1$  for even-even nuclei, while for odd- $A$  nuclei it is  $s = \pm i$ . However, experimental observation of two sets of parity doublet bands has been reported only in a few even-even [8, 20] and odd- $A$  [21, 22] nuclei. Particularly, for odd- $Z$  nuclei, it is not yet reported.

The La ( $Z = 57$ ) isotopes with  $A \sim 140$ , the seven valence protons above  $Z = 50$  closed shell show interesting features of the evolution from prolate deformation to the onset of octupole collectivity, as a function of neutron number. The neutron-rich La ( $Z = 57$ ) isotopes are predicted to lie within a region of mixed quadrupole-octupole deformation [18, 23, 24]. A competition between the symmetric and asymmetric shapes has also been pointed out in  $^{145}\text{La}$  [21]. Above  $N = 82$ ,  $^{140-142}\text{La}$  isotopes are expected to lie in a transitional region, where the interplay of prolate deformation and octupole collectivity is expected to evolve. On the other hand,  $^{143}\text{La}$  ( $N=86$ ) lies near the lower edge of the neutron number of this island, where the presence of octupole collectivity was reported [25]. The octupole collectivity is expected to increase towards  $N = 88 - 90$  (region of maximum collectivity), however in  $^{146,147}\text{La}$  ( $N = 89, 90$ ), it is reported to be weakened [26]. Thus, to understand the onset of octupole deformation in the La isotopic chain and to search for parity doublet bands corresponding to both simplex quantum numbers, investigations on high-spin states in the La isotopes above  $N = 82$  are necessary. While the heavier neutron-rich La isotopes have been studied and characterized through high-fold  $\gamma$ -ray spectroscopy produced in  $^{252}\text{Cf}$  spontaneous fission, the lighter La isotopes just above  $N = 82$  are difficult to access. In particular, the high spin states in  $^{140,141}\text{La}$  from in-beam spectroscopy, have not yet been characterized and several ambiguities exist on the high spin structures of  $^{142,143}\text{La}$ . Recent measurements of neutron separation energies obtained from new precision mass measurement [27] have shown the strongest change of two-neutron separation energy in the periodic table between  $N = 92$  and  $N = 94$  in La nuclei indicating more interesting aspects in this isotopic chain.

Here, we report the first identification of a pair of parity doublet structures in  $^{143}\text{La}$  and the high-spin level structures of  $^{140-142}\text{La}$  isotopes. The excited high spin states of these isotopes were measured using  $\gamma$ -ray spectroscopy, through two complementary techniques, combining isotopic identification of the fission fragments and high-fold  $\gamma$ -ray correlations. Further, the previously reported high-spin states in  $^{142}\text{La}$  [28] are now reassigned to  $^{143}\text{La}$  based on unambiguous isotopic identification.

## II. EXPERIMENT

The excited states and the  $(A, Z)$  identified  $\gamma$  rays of  $^{140-143}\text{La}$  isotopes have been investigated using two complimentary fission experiments, *viz.*, (i) prompt  $\gamma$ -ray spectroscopy from fusion-fission and transfer-induced fission reactions in inverse kinematics, using a  $^{238}\text{U}$  beam of energy 6.2 MeV/u, on a  $^9\text{Be}$  target (thicknesses  $1.6 \mu\text{m}$  and  $5 \mu\text{m}$ ) at Grand Accélérateur National d'Ions Lourds (GANIL), France; and (ii) high statistics three-fold  $\gamma - \gamma - \gamma$  and four-fold  $\gamma - \gamma - \gamma - \gamma$  coincidence data from the spontaneous fission of  $^{252}\text{Cf}$  using the Gammasphere, at LBNL, USA. These two complementary methods were combined earlier for the study of neutron-rich Pr [6], Pm [29] and Y [30] isotopes.

In the experiment at GANIL, the  $(A, Z)$  identification of the fission fragments was obtained using the large acceptance magnetic spectrometer VAMOS++ [31, 32]. It was placed at an angle of  $20^\circ$  with respect to the beam axis [31–33]. The  $Z$  identification was obtained from  $\Delta E - E$ , using the ionization chamber at the focal plane of VAMOS++. The time of flight of each fragment was measured between a Dual Position-Sensitive Multi-Wire Proportional Counter (DPS-MWPC) [34], placed behind the target at the entrance of VAMOS++, and the MWPC placed at the focal plane. The focal plane detector system also includes two drift chambers (DC) for tracking the trajectory of the ions. The mass number ( $A$ ), atomic number ( $Z$ ), atomic charge ( $Q$ ) and the velocity of the fission fragments were determined on an event-by-event basis. The mass-to-charge ratio ( $M/Q$ ) was obtained from the reconstructed magnetic rigidity ( $B\rho$ ) and the velocity of the fragment. The prompt  $\gamma$  rays, emitted in coincidence with a given fission fragment, were detected using the AGATA setup at GANIL [35], placed 13.5 cm from the target. The Doppler correction for the  $\gamma$  rays was made using the velocity of the emitting fragments and the corresponding position of the  $\gamma$  rays in AGATA. The  $\gamma$ -ray energy uncertainties after Doppler correction, are typically  $\pm 0.2$  keV,  $\pm 0.5$  keV and  $\pm 1$  keV around 200 keV, 500 keV and 1 MeV respectively. The data were collected demanding a coincidence between the prompt  $\gamma$  rays and DPS-MWPC conditioned by the MWPC in the focal plane within 300 ns. Further details and identification of fragments and corresponding coincidence  $\gamma$  rays in AGATA are given in Ref. [33, 36].

The high-fold  $\gamma$ -coincidence data was obtained using 101 HPGe detectors of the Gammasphere setup at LBNL. A  $62\text{-}\mu\text{Ci}$   $^{252}\text{Cf}$  source was sandwiched between two Fe foils of thickness  $10 \text{ mg/cm}^2$ . The fission fragments and  $\alpha$  particles were stopped by foils, while neutrons and  $\beta$  particles were partially moderated and absorbed by the foils and a 7.6 cm diameter plastic ball. The data were sorted into  $\gamma - \gamma - \gamma$  and higher fold  $\gamma$  events to form a cube (three-fold) and more recently in a hyper-cube (four-fold), and were analyzed using the RADWARE package [37]. More details of the experiment and analysis procedures can be found in [6].

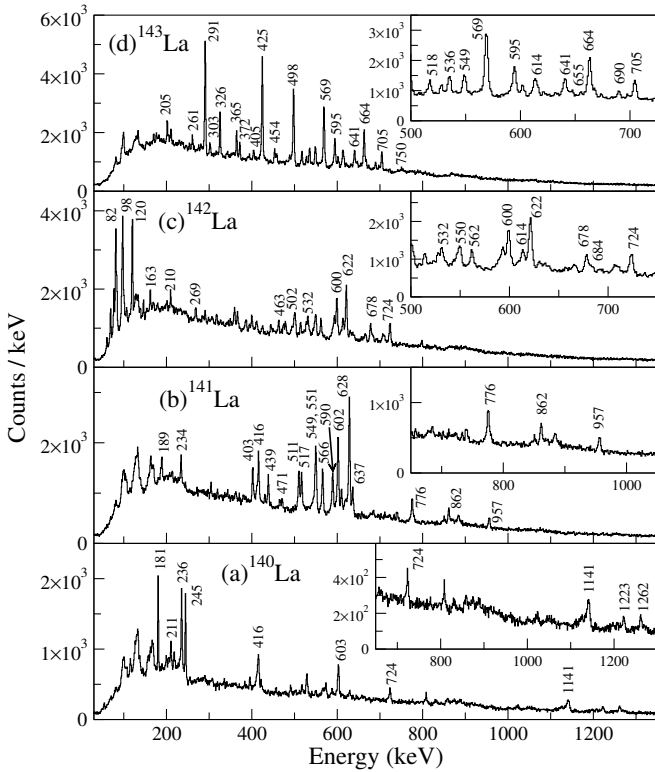


FIG. 1: (A,Z) gated Doppler corrected ‘singles’  $\gamma$ -ray spectra of  $^{140-143}\text{La}$ , detected in AGATA, from the fragment- $\gamma$  coincidences in  $^{238}\text{U}+^{9}\text{Be}$ -induced fission data. The insets show part of the spectra in an expanded scale.

### III. RESULTS

The present work reports on the in-beam prompt  $\gamma$  rays from high spin states of isotopically identified  $^{140-143}\text{La}$  nuclei. The  $\gamma$  rays decaying from the low-lying states of  $^{140-142}\text{La}$  have been known earlier either from  $\beta$ -decay [38–40] or from  $(n,\gamma)$  reactions [41]. For  $^{143}\text{La}$ , the high spin states are known from the study of spontaneous fission of  $^{252}\text{Cf}$  [25, 42]. The isotopically identified Doppler corrected  $\gamma$ -ray spectra of  $^{140-143}\text{La}$  isotopes, observed in the present work using AGATA, are shown in FIG. 1. In the case of  $^{142-143}\text{La}$ , it was additionally possible to use the high fold  $\gamma$  coincidence cube and hypercube data, obtained using Gammashpere. The details of the level structure of the La isotopes reported in the present work are given in the following subsections.

#### A. $^{140}\text{La}$

The present work reports on the first measurements of  $\gamma$  rays from high-spin states of  $^{140}\text{La}$ . The previous studies on  $^{140}\text{La}$  reported the  $\gamma$  rays depopulating mostly the low spin excited states, observed either in  $\beta$ -decay [38] or from  $(n,\gamma)$  reactions [41].

The Doppler corrected  $\gamma$ -ray spectrum of  $^{140}\text{La}$ , mea-

sured in AGATA, is shown in FIG. 1(a). The proposed level scheme of  $^{140}\text{La}$ , as obtained from the present work, is shown in FIG. 2. The energies shown are adopting the placement of 235.8 keV transition in Ref. [41], and following the energy systematics of neighbouring  $N = 83$  isotope  $^{138}\text{Cs}$ . The  $\gamma$  rays, assigned to  $^{140}\text{La}$ , along with their relative intensities and the level energies, obtained from the (A,Z) gated spectra are shown in Table. I in the appendix.

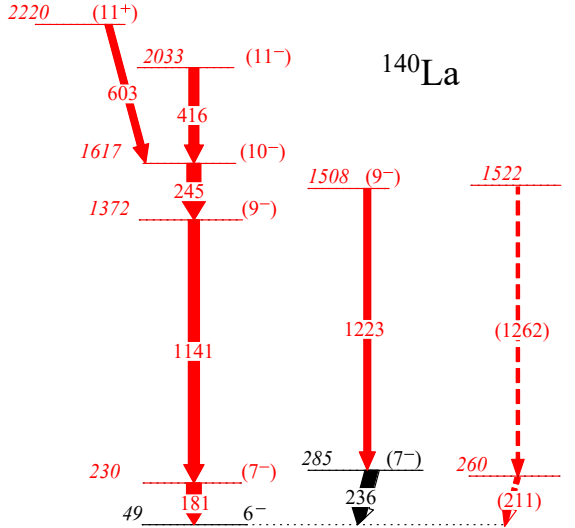


FIG. 2: Level scheme of  $^{140}\text{La}$ , obtained from the present work. The  $6^-$  level was reported in  $\beta$ -decay [38] and  $(n,\gamma)$  reactions [41]. The new transitions from the present work are marked in red colour. The  $211$  and  $1262$  keV  $\gamma$  transitions are denoted as dashed lines to indicate the tentative nature of their placement (see text). Their assignment to  $^{140}\text{La}$  is confirmed from the (Z,A) gated spectrum.

The prompt coincidence spectra with coincidence gates on the  $181$  keV and  $1223$  keV  $\gamma$  rays, obtained using AGATA, are shown in FIG. 3. The presence of the strong  $245$ ,  $416$ ,  $603$  and  $1141$  keV transitions can be clearly seen. The  $603$  keV transition is found to be in coincidence with all these transitions, except the  $416$  keV transition. Thus, the  $181$ ,  $1141$ ,  $245$  and  $416$  keV transitions are placed in a cascade, on the basis of their mutual coincidence relations and relative intensities, whereas, the  $603$  keV transition is placed in parallel with the  $416$  keV transition. The intense  $236$  keV  $\gamma$ -ray, observed in the singles spectrum, is found to be in coincidence only with the  $1223$  keV  $\gamma$ -ray, as shown in FIG. 3. Therefore, the  $236 - 1223$  keV coincidence cascade is placed in parallel with the  $181 - 1141$  keV band  $\gamma$  rays. The other two weak transitions  $1262$  and  $211$  keV, were found to have a weak coincidence only with each other and therefore are tentatively placed as a parallel cascade. Due to this reason the  $211$  and  $1262$  keV transitions are denoted as dashed lines. Though their assignment to  $^{140}\text{La}$  is confirmed from the mass gated spectrum, but their placement in level scheme is tentative due to lack of coincidence statistics. The  $724$  keV  $\gamma$  ray, observed in the singles  $\gamma$ -ray

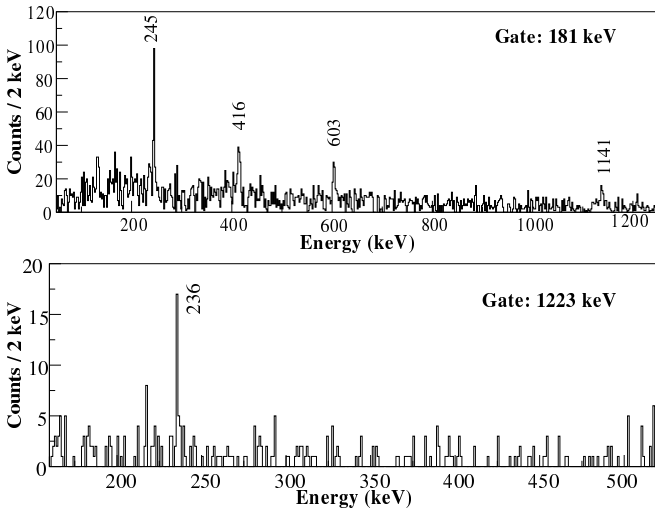


FIG. 3: Coincidence spectrum corresponding to the 181 keV (upper panel) and 1223 keV (lower panel)  $\gamma$ -rays of  $^{140}\text{La}$ , obtained from the  $^{238}\text{U} + ^9\text{Be}$ -induced fission data.

spectrum (FIG. 1(a)), obtained in coincidence with the  $^{140}\text{La}$  fragment, does not show any coincidence with the other observed  $\gamma$  rays. A 722.5 keV transition was reported in a  $(n, \gamma)$  study [41], as decaying to the 48.8 keV  $6^-$  level. The 724 keV  $\gamma$  ray, observed in the present work, could be the same transition, decaying directly to the  $6^-$  level in parallel with the other transitions.

Earlier studies on  $^{140}\text{La}$  from thermal neutron capture reactions [41] also reported two parallel transitions of 180.8 and 235.8 keV, as decaying from the 284.6 keV level, to the two different  $6^-$  levels at 103.8 keV and 48.8 keV, respectively. However, these two  $\gamma$  rays were not observed in  $\beta$ -decay [38]. The study of low-lying states of  $^{140}\text{La}$  by  $(d, p)$  reaction [43] also reported the states at 284.6 keV and 48.8 keV and assigned the spin-parity of  $7^-$  and  $6^-$ , respectively. It is found that, the intensity of 180.8 keV  $\gamma$  ray with respect to that of 235.8 keV  $\gamma$  ray is only 5%, as reported in Ref. [41]. This intensity ratio is much less compared to that of the 181 keV  $\gamma$ -ray, observed in the present work (produced with almost equal intensity as that of the 235.8 keV transition). Thus, the 181 keV transition, observed in the present work and the 180.8 keV, observed in Ref. [41], are most likely not the same. Further, from the present  $\gamma - \gamma$  coincidence data, the 181 and 236 keV transitions cannot be placed as decaying from the same level, as the  $\gamma$  rays of 245, 416, 603 and 1141 keV, placed above the 181 keV  $\gamma$ -ray, are found to be in coincidence only with 181 keV, but not with 236 keV  $\gamma$ -ray. Therefore, in the present work, the 181 and 236 keV  $\gamma$  rays are placed as decaying from two different levels. The 181 keV transition, observed in the present work, is placed as decaying to the same  $6^-$  level at 48.8 keV, though its placement as decaying to any of the other known low-lying levels in  $^{140}\text{La}$  cannot be ruled out. The 236 keV  $\gamma$ -ray is considered to decay from a  $7^-$  level to a  $6^-$  level, as reported in Ref. [41, 43]. The

spin-parity assignments of the state decaying by 181 keV transition and the higher spin states corresponding to the  $\gamma$ -ray cascades of 245, 416, 603 and 1141 keV, are made on the basis of the systematics of the neighbouring  $N = 83$  isotones  $^{138}\text{Cs}$  [44]. In the present work, the induced fission data can only determine the energy levels and intensities of the transitions. The calculations discussed later in the text support the tentative spin/parity assignments that have been made.

## B. $^{141}\text{La}$

The present work reports on the in-beam  $\gamma$  rays from high spin states in  $^{141}\text{La}$ , for the first time. Prior to the present measurements, the information on the excited states of  $^{141}\text{La}$  at low spin was mainly obtained from the  $\beta$ -decay of  $^{141}\text{Ba}$  [39, 45]. A recent work [39] reports detailed measurements of  $\gamma - \gamma$  coincidence, angular correlation of decay  $\gamma$  rays and  $\beta$ -feeding to low-lying positive and negative parity states. None of these  $\gamma$  rays of  $^{141}\text{La}$  are observed in the present study.

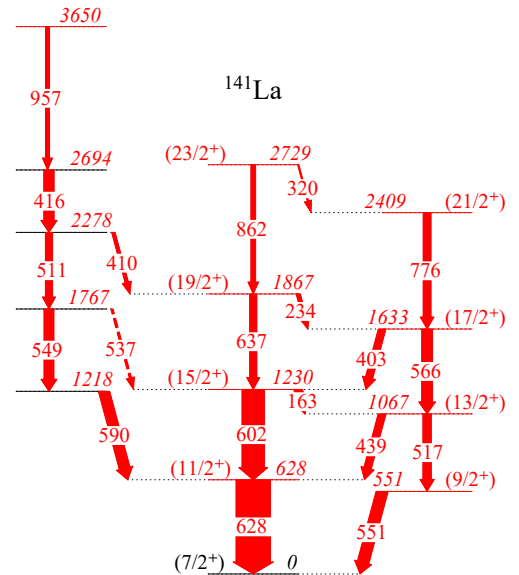


FIG. 4: Level scheme of  $^{141}\text{La}$ , obtained from the present work. The new transitions from the present work are marked in red colour.

FIG. 4 shows the proposed level scheme of  $^{141}\text{La}$ , obtained from the present work. The  $\gamma$  rays placed in the level scheme are identified on the basis of the  $\gamma$  rays detected in coincidence with the  $^{141}\text{La}$  fragments. The corresponding  $\gamma$  spectrum is shown in FIG. 1(b). A majority of the  $\gamma$  rays observed in this spectrum are placed in the level scheme (FIG. 4), on the basis of prompt  $\gamma - \gamma$  coincidence and their relative intensities. The  $\gamma$  rays, assigned to  $^{141}\text{La}$ , along with their relative intensities and the level energies, obtained from the  $(A, Z)$  gated spectra are shown in Table. II in the appendix.

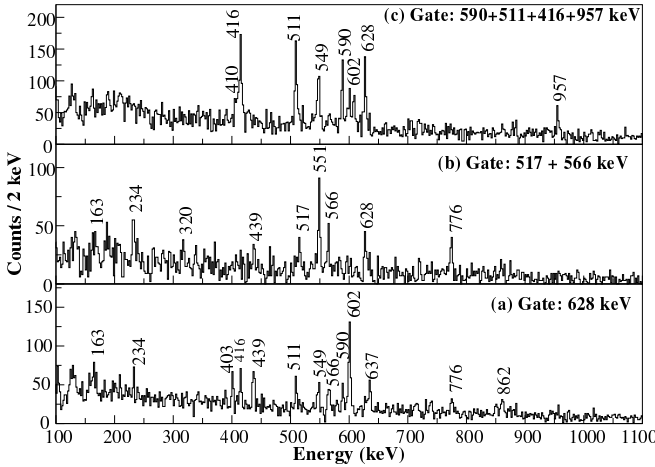


FIG. 5: Coincidence spectrum corresponding (a) the 628 keV gate, (b) the added gates of 517 and 566 keV  $\gamma$  rays, (c) the added gates of 590, 511, 416 and 957 keV  $\gamma$  rays of  $^{141}\text{La}$ , obtained from  $^{238}\text{U} + ^9\text{Be}$ -induced fission data.

The coincidence spectra corresponding to different  $\gamma$ -ray coincidence conditions are shown in FIG. 5(a-c). The coincidence spectrum corresponding to the gate of the most intense  $\gamma$ -ray of 628 keV, observed in  $^{141}\text{La}$ , is shown in FIG. 5(a). It can be seen that except for the 551 and 517 keV transitions, which are placed in parallel to the band built on the 628 keV  $\gamma$ -ray, all other  $\gamma$  rays observed in the single spectrum are found to be in coincidence with the 628 keV  $\gamma$  ray. The 628 – 602 – 637 – 862 keV  $\gamma$  rays form the main cascade in the level scheme of  $^{141}\text{La}$ . The 549 and 551 keV transitions cannot be separated in the singles spectrum (FIG. 1(b)). But the summed coincidence gates of 517 and 566 keV (FIG. 5(b)) and the summed coincidence gates of 590 – 511 – 416 – 957 keV  $\gamma$ -ray cascade (FIG. 5(c)), clearly separate 551 keV and 549 keV transitions. Thus, the 549 keV and 551 keV  $\gamma$  rays are placed in two different cascades. The set of transitions, consisting of 590 – 549 – 511 – 416 – 957 keV show mutual coincidences, and all these transitions are in coincidence with the 628 keV  $\gamma$ -ray. The 511, 416, and 957 keV transitions also show a weak coincidence with the 602 keV  $\gamma$ -ray, which indicates a possible connection between the two cascades. It is found that the 2278 keV level is connected with the 1867 keV ( $19/2^+$ ) state of the main yrast cascade through a 410 keV  $\gamma$ -ray. However, the connection of the 1767 keV state to the 1230 keV ( $15/2^+$ ) state of the yrast cascade could not be established and thus is shown as a tentative transition of 537 keV in the level scheme (FIG. 4). It may be noted that, a similar cascade of transitions, connecting to each level of the yrast sequence, has also been identified in the neighbouring  $N = 84$  isotope  $^{139}\text{Cs}$  [46]. The tentative spin-parity assignments of the new levels of the yrast band structures in  $^{141}\text{La}$  are made on the basis of the systematics of  $N = 84$  isotones of Cs and I nuclei [46].

### C. $^{142}\text{La}$

The present work reports on the de-excitation  $\gamma$  rays from higher spin states in  $^{142}\text{La}$ . The isotopically tagged prompt  $\gamma$  rays in  $^{142}\text{La}$  are shown in FIG. 1(c). The low spin states of  $^{142}\text{La}$  up to 1.5 MeV excitation have been reported earlier following the  $\beta$ -decay of  $^{142}\text{Ba}$  [40]. A set of cascade  $\gamma$  rays was reported in Ref. [28], as belonging to  $^{142}\text{La}$ , from  $^{252}\text{Cf}$  spontaneous fission, but none of the  $\gamma$  rays are observed in the (A, Z) gated spectrum of the present work (FIG. 1(c)).

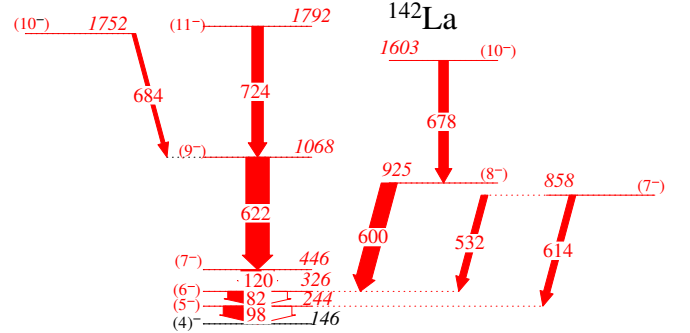


FIG. 6: Level scheme of  $^{142}\text{La}$ , obtained from the present work. The 146 keV ( $4^-$ ) level was reported in  $\beta$ -decay [40]. The new transitions from the present work are marked in red colour.

The new level scheme of  $^{142}\text{La}$ , proposed from the present work is shown in FIG. 6. The  $\gamma$  rays, assigned to  $^{142}\text{La}$ , along with their relative intensities and the level energies, obtained from the (A,Z) gated spectra are shown in Table. III in the appendix.

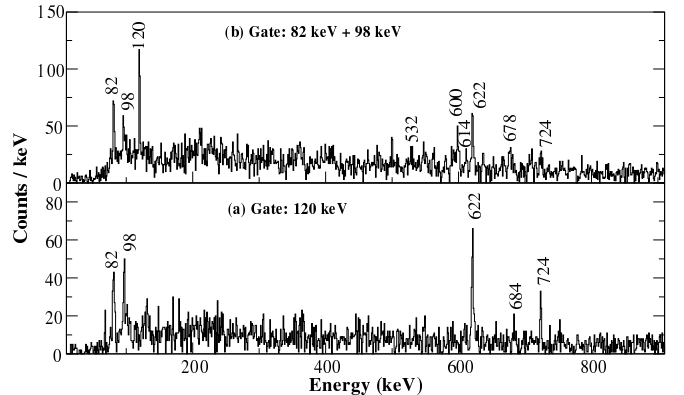


FIG. 7: Coincidence spectra corresponding to the (a) added gates of 82 and 98 keV  $\gamma$  rays using the data from AGATA, (b) gate of 120 keV  $\gamma$  rays in  $^{142}\text{La}$ , as obtained from the  $^{238}\text{U} + ^9\text{Be}$ -induced fission data.

A coincidence spectrum corresponding to the sum gate 82 and 98 keV  $\gamma$  rays using the data from AGATA is shown in FIG. 7(a). It can be seen that most of the  $\gamma$  rays of  $^{142}\text{La}$  are in coincidence with 82 and 98 keV transitions. FIG. 7(b) shows the coincidence spectrum of 120 keV  $\gamma$  ray, in which only the transitions correspond-

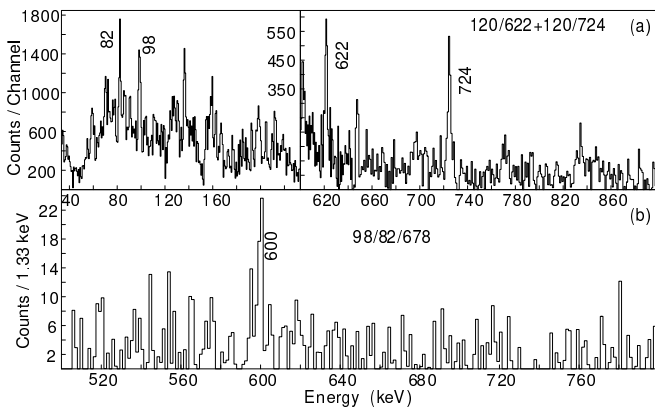


FIG. 8: Coincidence spectra corresponding to the (a) added double gates of 120-622 and 120-724, (b) triple gates of 98-82-678 keV  $\gamma$  rays in  $^{142}\text{La}$ , obtained from  $^{252}\text{Cf}$  fission using Gammasphere.

ing to the yrast cascade are present. The coincidence relations of the other observed  $\gamma$  rays, such as, 502, 550 and 562 keV, were not clear and therefore these are not placed in the level scheme. However, their identification as belonging to the  $^{142}\text{La}$  is confirmed by the fragment- $\gamma$  coincidence, shown in FIG. 1(c). In addition to the coincidence relationship obtained using VAMOS-AGATA the high-fold  $\gamma$ -ray coincidences, obtained using Gammasphere have also been used. Such a combined analysis was only possible for  $^{142,143}\text{La}$  isotopes in the present work due to the relatively lower yields of  $^{140,141}\text{La}$  in the spontaneous fission of  $^{252}\text{Cf}$ . These high-fold  $\gamma$ -ray coincidence cube and hypercube, made from the coincident data of the Gammasphere array have been utilized to further confirm the placement of various cascade transitions in  $^{142}\text{La}$ . FIG. 8(a) shows the summed double gates of 120/622 keV and 120/724 keV transitions and, the four-fold coincidence gates of 98/82/678 keV transitions from the hypercube data are shown in FIG. 8(b). In part (a), it can be seen that the strong 82, 98, 622 and 724 keV transitions, observed in the data from  $^{238}\text{U}+^{9}\text{Be}$  reaction (FIG. 1 and 7) are also confirmed by the  $^{252}\text{Cf}$  spontaneous fission. The presence of the 600 keV transition can be clearly seen in the four-fold coincidence of the 98/82/678 keV transitions.

In  $^{252}\text{Cf}$  spontaneous fission data, weak evidence of  $\approx 68$  and  $78$  keV transitions are also seen. A previous  $^{142}\text{Ba}$   $\beta$ -decay study [40] reported the 68.3-77.6 and 69.7-77.6 keV cascades to the ground state depopulating the 145.9 and 147.3 keV levels, respectively. In Ref. [40], only the 146 keV level was tentatively assigned to  $(4)^-$ . The level scheme shown in the Fig. 6 is built on this  $(4)^-$  state. Based on the systematic comparison with  $A = 85$  isotones and the shell model calculations discussed in the next section, the tentative spin-parity of the excited states in  $^{142}\text{La}$  has been assigned.

## D. $^{143}\text{La}$

### 1. Level Structure

The level scheme of  $^{143}\text{La}$  was earlier reported in Ref. [25, 42]. FIG. 9 shows the new and extended level scheme of  $^{143}\text{La}$  obtained in this work. Bands (1), (3) and (6) in FIG. 9 were reported in Ref. [25, 42]. The strong transitions in these Bands are confirmed in the A and Z gated spectrum, shown in FIG. 1. The  $\gamma$  rays, assigned to  $^{143}\text{La}$ , along with their relative intensities and the level energies, obtained from the (A,Z) gated spectra are shown in Table. IV in the appendix.

Using a sum gate of 291 and 498 keV  $\gamma$  - ray transitions (FIG. 10), the previously reported transitions of 291, 326, 454, 498, 518, 536, 570, 595, 615, 641 and 664 keV can be clearly identified. The transitions and levels in Bands (2), (4) and (5) in FIG. 9 were assigned to  $^{142}\text{La}$  in Ref. [28]. These Bands in FIG. 9 are now assigned to  $^{143}\text{La}$  in the present work, using the A and Z gated isotopically identified  $\gamma$  - rays. It is clear from FIG. 1, that, the 425, 549, 569 and 705 keV transitions are seen in the A and Z gated spectrum corresponding to  $^{143}\text{La}$ , but not in the corresponding spectrum for  $^{142}\text{La}$ . Furthermore, in FIG. 11(a) the triple gate of 291/498/705 keV transitions, shows the 205 keV linking transition from Band (2) to Band (1). In FIG. 11(b), using triple gates of the 425/569/326 keV transitions, the 459 keV linking transition from Band (1) to Band (2) can be seen. The strong 595 keV transition in Band (6) is also seen in FIG. 12. These coincidence spectra from  $^{252}\text{Cf}$  spontaneous fission data assign these  $\gamma$ -rays to be the linking transitions from Bands (1) and (2). This also confirms that these transitions are indeed in the same nucleus and not two different nuclei, as assigned in Ref. [25, 28, 42].

Spectra in FIG. 12 show the new transitions in  $^{143}\text{La}$ , based on coincidences from  $^{252}\text{Cf}$  spontaneous fission data. In part (a), a summation of two double gates on 291/498 and 498/664 keV transitions, shows new higher energy 724, 750, and 975 keV transitions. In part (b), by adding 291/498/664, 291/498/326 and 498/664/326 keV triple gates, the new 424 keV transition, as well as the previously identified 203, 291, 326, 405 and 595 keV transitions, can be seen. Thus, the unique identification of  $\gamma$  rays in the case of a nucleus with low yields and with no known  $\gamma$  transitions, can be challenging using only the  $\gamma$ -ray coincidences and the cross-coincidence relationships with the complementary fission fragments. Hence, the combination of two very powerful techniques used in this work is the key for obtaining detailed spectroscopy of such hard-to-populate nuclei.

### 2. Angular Correlation Measurements

In the present work, the relatively large yields of  $^{143}\text{La}$  in  $^{252}\text{Cf}$  spontaneous fission permitted the measurement of  $\gamma$ - ray angular correlations work, and the results are

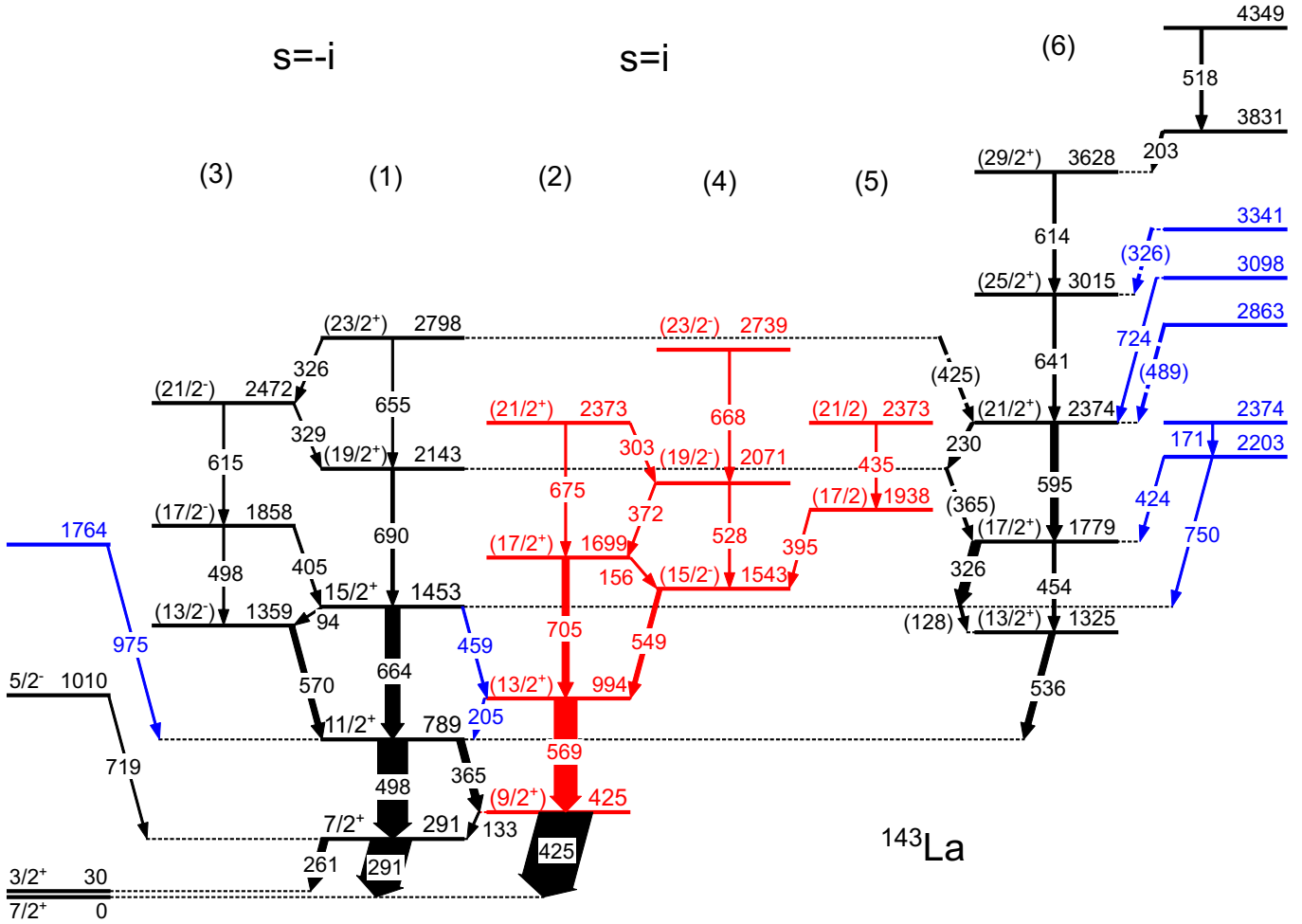


FIG. 9: Level scheme of  $^{143}\text{La}$ , obtained from the present work. Transitions in black were reported in Ref. [25, 42] from spontaneous fission of  $^{252}\text{Cf}$ . The 1010 keV level and its decay by 719 keV transition was reported only from  $\beta$ -decay [47]. Transitions in blue and red are newly assigned  $^{143}\text{La}$ . The transitions in red were earlier misidentified as belonging to  $^{142}\text{La}$  in Ref. [28].

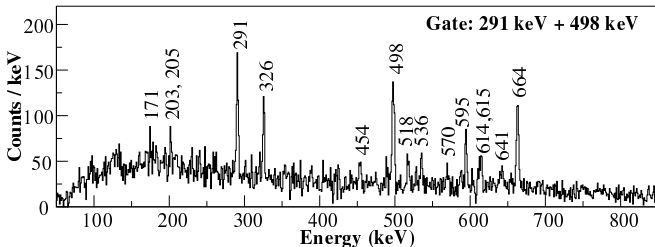


FIG. 10: Coincidence spectra corresponding to the summed gates of the 291 and 498 keV  $\gamma$  rays in  $^{143}\text{La}$ , as obtained from the  $^{238}\text{U}+^{9}\text{Be}$  induced-fission data.

shown in FIG. 13 and Table I. These are used to determine the  $J^\pi$  of the states in  $^{143}\text{La}$ . These newly measured angular correlations are combined with previous measurements for the  $\beta$ -decay of  $^{143}\text{Ba}$  [47] to assign the  $J^\pi$  of the excited states of  $^{143}\text{La}$ .

Results from the  $\beta$ -decay relevant to the level scheme

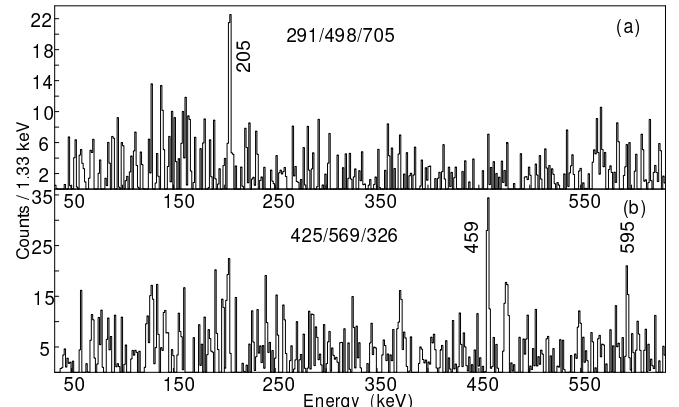


FIG. 11: Coincidence spectra corresponding to the triple gates of (a) 291-498-705 keV and (b) 425-569-326 keV  $\gamma$  rays in  $^{143}\text{La}$ , as obtained from the  $^{252}\text{Cf}$  fission data.

from the present work are briefly summarized below. The

TABLE I: Angular correlations of cascades in  $^{143}\text{La}$ . Values from  $^{143}\text{Ba}$   $\beta$  decay in Ref. [47] are also included and labeled with an ‘\*’. The spin assignments from the present work are marked with ‘\*\*’. All the cascades for the present angular correlations are chosen in such a way that one of the transitions is either E2 or E1 so that it has minimum (zero) mixing. The possible mixing ratio ( $\delta$ ) for the other transition is quoted comparing the calculated (theoretical) angular correlation coefficients ( $A_2$  and  $A_4$ ) for different  $\delta$  with the experimental values.

cascade (keV)	$A_2/A_4$ exp.	$A_2/A_4$ theo.	$\delta(\text{E2}/\text{M1})$	possible decay pattern
719-291	-0.23(4)/none*	-0.14/0	0	$5/2^-$ (E1) $3/2^+$ (E2) $7/2^+$
			6.2(29) or 0.31(8)	$5/2^-$ (E1) $5/2^+$ (E2/M1) $7/2^+$
			0.44(30)	** $5/2^-$ (E1) $7/2^+$ (E2/M1) $7/2^+$
498-291	0.143(25)/-0.029(38)	(within $2\sigma$ )	-0.87(56)	$9/2^+$ (E2) $5/2^+$ (E2/M1) $7/2^+$
			0.42(33)	** $11/2^+$ (E2) $7/2^+$ (E2/M1) $7/2^+$
719-261	-0.14(3)/none*	(within $2\sigma$ )	0.78(54)	$5/2^-$ (E1) $3/2^+$ (E2/M1) $3/2^+$
			-3.7(5) or 0.024(37)	$5/2^-$ (E1) $5/2^+$ (E2/M1) $3/2^+$
			-0.15/0	** $5/2^-$ (E1) $7/2^+$ (E2) $3/2^+$
498-664	0.061(23)/-0.001(35)	0.10/0.01 (within $2\sigma$ )		** $15/2^+$ (E2) $11/2^+$ (E2) $7/2^+$
326-664	0.025(43)/-0.013(65)		5.2(20) or 0.16(7)	** $17/2^+$ (E2/M1) $15/2^+$ (E2) $11/2^+$

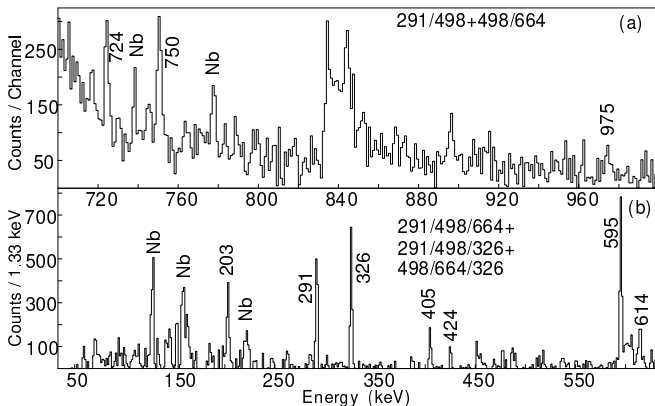


FIG. 12: Coincidence spectra corresponding to the (a) added double gates of 291-498 and 498-664, (b) added triple gates of 291-498-664, 291-498-326 and 498-664-326  $\gamma$  rays in  $^{143}\text{La}$ , as obtained from the  $^{252}\text{Cf}$  fission data.

ground state of  $^{143}\text{La}$  was assigned a  $J^\pi = 7/2^+$  based on the logft value and systematics. The state at 30 keV was assigned a  $J^\pi = 3/2^+$  based on the E2 character of the transition to the ground state, obtained from the measurement of internal conversion coefficients. The state at 1010 keV level was assigned  $J^\pi = 5/2^-$  based on the logft value and the decay pattern. These assignments are adopted in the present work. Foller *et al.* [47] further reported other angular correlation measurements of transitions from low-spin non-yrast states (generally relatively poorly populated in a fission reaction) that can be used to obtain the  $J^\pi$  of states populated in the present work. The angular correlation for the 719 – 291 keV transitions (719 keV transition from the  $5/2^-$  state at 1010 keV populates the state at 291 keV, which in turn feeds the  $7/2^+$  ground state) was used to determine the  $J^\pi$  of the state

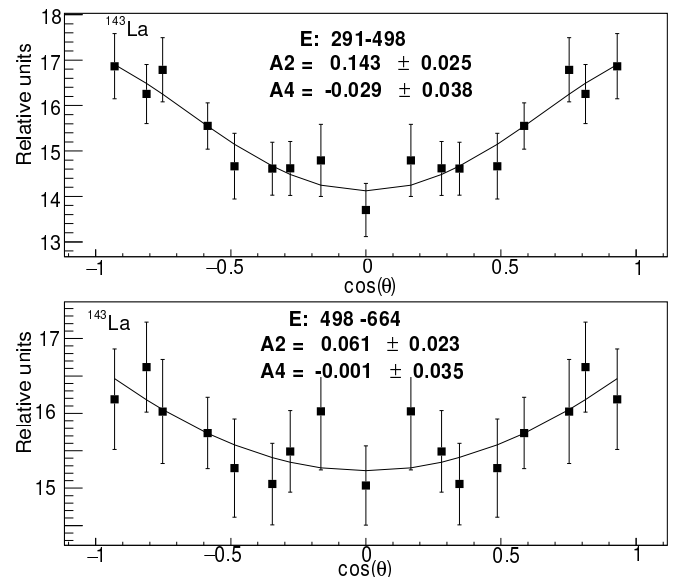


FIG. 13: Angular correlation of the 291-498 keV cascade (upper panel) and the 498 – 664 keV cascade (lower panel) in  $^{143}\text{La}$ , as obtained from the  $^{252}\text{Cf}$  spontaneous fission data.

at 291 keV. The 261 and 291 keV transitions (see FIG. 9) were assigned as mixed (E2/M1) transition from the measured internal conversion coefficients. Thus, the possible values of the  $J^\pi$  of the state at 291 keV are  $3/2^+$ ,  $5/2^+$  or  $7/2^+$ . It should be noted that for the 261 keV transition from the state at 291 keV to the  $3/2^+$  state at 30 keV level, the measured  $\alpha_k$  value is in better agreement with the calculated value for an E2 transition. For an assignment of  $3/2^+$  spin for the state at 291 keV in the cascade  $5/2^-$  (719, E1)  $3/2^+$  (291, E2)  $7/2^+$ , the mixing ratio ( $\delta$ ) is very small. The calculated angular correlation co-

efficients for  $\delta=0$ , do not match the experimental values given in Table I, and thus we can discard the assignment of  $3/2^+$  spin for the state at 291 keV. Among the other two possibilities ( $5/2^+$  or  $7/2^+$ ) the calculations match the experimental angular correlation coefficients for different mixing ratios of 291 keV transition. The values of the mixing ratio ( $\delta$ ) of the 291 keV transition are found to be 6.2(29) or 0.31(8) in the case of  $J^\pi = 5/2^+$  and 0.44 if  $J^\pi = 7/2^+$ .

In Table I the measured angular correlation of the 498 – 291 keV cascade (Band 1) is compared with the theoretical values assuming a pure E2 character (zero mixing) for the 498 keV transition. For an assignment of  $J^\pi$  of  $5/2^+$  for the level at 291 keV, the experimental values of angular correlation coefficients are within  $2\sigma$  of the calculated values for a  $\delta = -0.87(56)$ . On the other hand, for an assignment of  $J^\pi$  of  $7/2^+$ , the experimental values are well within the limit of theoretical values for  $\delta = 0.42(33)$ . The angular correlation coefficients for 719 – 291 keV cascade, reported in [47] and that for 498 – 291 keV cascade from the present work, show a consistent value of  $\delta$  of 0.44(30) and 0.42(33) respectively (Table I), for the 291 keV transition only if the 291 keV level has a spin-parity of  $7/2^+$ . The assignment of  $7/2^+$  to this level is further validated by the angular correlation of the 719 – 261 keV cascade as shown in Table I. Among the three possible spin sequences, the theoretical angular correlation coefficients ( $-0.15/0$ ) for the E1-E2 (both  $\delta = 0$ )  $5/2^-$  719 (E1)  $7/2^+$  261 (E2)  $3/2^+$  cascade. The  $7/2^+$  assignment also corroborates with the E2 nature of the 261 keV transition, decaying from the same state. Based on the above angular correlation analysis, the spin-parity of the 291 keV level is unambiguously shown to be  $7/2^+$ .

The angular correlation, shown in the lower panel of FIG. 13, for the 498 – 664 cascade (Band 1), is consistent with a pure E2-E2 cascade. As the state at 789 keV was not observed in  $\beta$ -decay [47], it indicates its high spin character. The E2 character of the 498 and 664 keV transitions are also in line with those in neighbouring nuclei (discussed in the next section). The angular correlation of the 326 – 664 cascade (Band 6 and Band 1) was also measured in the present work and was found to have a positive A2 value. Assuming the 664 keV transition to be of an E2 character, the positive A2 value yields a mixed E2/M1 character for the 326 keV transition. This indicates that Band (3) has a positive parity as assigned in Ref. [25].

#### IV. DISCUSSION

The systematics for the excited state for the  $N = 83$  to 86 of La and neighboring isotones are shown in Figs. 14, 15 and 16. Although the present induced fission data can only determine the excited energy levels from the transition coincidence relationships and their intensities, the energy systematics of isotones and the following

discussed shell model calculations support the tentative spin/parity assignments.

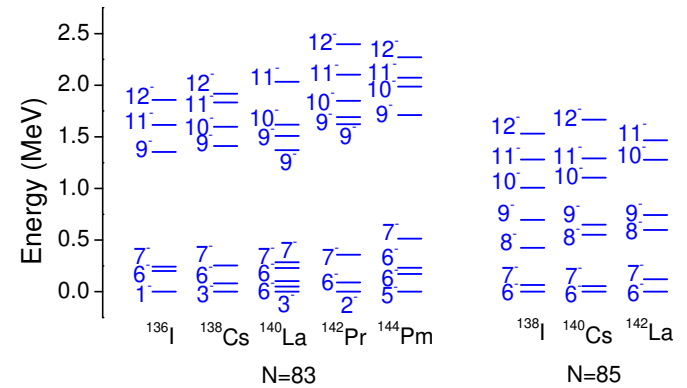


FIG. 14: Systematics of the excited states for even- $A$   $N = 83$  and  $N = 85$  isotones. For the  $N = 83$  isotones, the energies correspond to the excited states. For  $N = 85$  isotones, the energies are with respect to the lowest  $6^-$  level.

From the excitation energy pattern of the  $N = 83$  isotones (FIG. 14), it can be seen that the negative parity excited states identified in the present work for  $^{140}\text{La}$  follow well the systematics of the neighbouring isotones for  $Z = 53$  to  $Z = 61$  nuclei. The level sequence and spacing for these isotopes exhibit a strong similarity. The excitations up to spin  $10^-$  states are almost constant from  $^{136}\text{I}$  ( $Z = 53$ ) to  $^{140}\text{La}$  ( $Z = 57$ ). For  $^{142}\text{Pr}$  ( $Z = 59$ ) and  $^{144}\text{Pm}$  ( $Z = 61$ ), the higher spin states shift to relatively higher excitations. This could be due to the increasing collectivity related to the larger number of valence protons outside the  $Z = 50$  major shell closure.

The systematics of  $N = 85$  isotones for I ( $Z = 53$ ), Cs ( $Z = 55$ ) and La ( $Z = 57$ ) are also plotted in FIG. 14. Very limited data for  $^{144}\text{Pr}$  [6] is available and hence is not shown in the figure. A remarkable similarity is also observed for the excited states in  $N = 85$   $^{138}\text{I}$ ,  $^{140}\text{Cs}$ ,  $^{142}\text{La}$ . These systematics were used in the tentative assignment of the spin-parity of the new high spin states observed in  $^{142}\text{La}$  in the present work.

In the case of  $N = 84$  isotones (FIG. 15), the yrast cascade patterns of all these isotopes from Sb ( $Z = 51$ ) to La ( $Z = 57$ ) are also very similar. The first excited state reported in these isotopes is  $5/2^+$ , the corresponding state is not observed in  $^{141}\text{La}$  from the present work and therefore not shown in FIG. 15. The other Band built on the 1218 keV level, observed in  $^{141}\text{La}$ , decays to the yrast Band at 628 keV ( $11/2^+$ ). This Band is not yet observed in the  $N = 84$  isotones of the other lower  $Z$  nuclei and therefore not shown in FIG. 15.

The systematics of the excited states of  $N=86$  isotones are shown in FIG. 16. The parity doublet structure observed in  $^{143}\text{La}$  in the present work is very similar to the parity doublet structure reported in neighbouring isotope  $^{141}\text{Cs}$ . In the case of I and Pm isotopes having the same neutron number, only positive parity bands are reported.

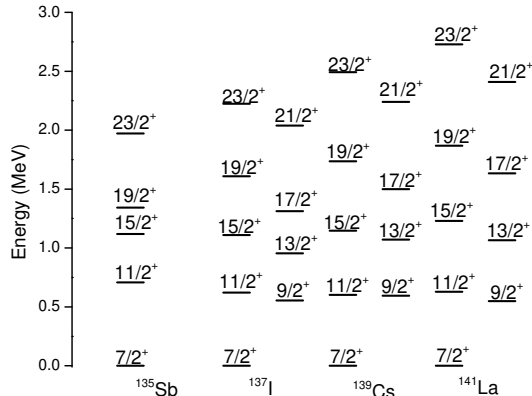


FIG. 15: Systematics of positive parity excited states (with respect to  $7/2^+$  state) for odd- $A$   $N = 84$  isotones.

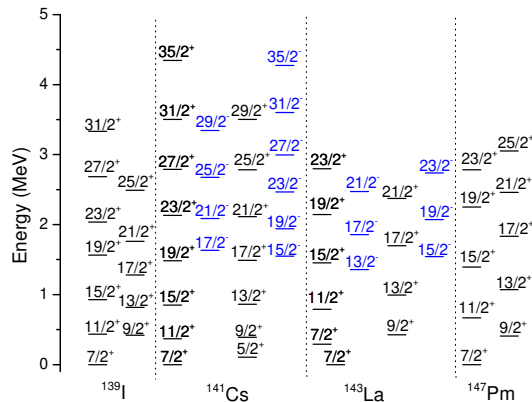


FIG. 16: Systematics of excited states for odd- $A$   $N = 86$  isotones. For  $^{143}\text{La}$ , only the states corresponding to the parity doublet structures are shown. The positive and negative parity states are shown in black and blue colour respectively.

### A. Shell Model Calculations

The shell model calculations presented here have been performed in the model space of  $50 \leq Z \leq 82$  and  $82 \leq N \leq 126$ . The effective Hamiltonian is based on the complete effective nuclear force  $V_{\text{MU}} + \text{LS}$  [48], which consists of the Gaussian central force, the  $\pi + \rho$  meson-exchange tensor force, and M3Y spin-orbit force [49].  $V_{\text{MU}} + \text{LS}$  has been successfully employed in the  $psd$  [50],  $sdpf$  [51],  $pfsdg$  regions [52], and the nearby regions of  $^{132}\text{Sn}$  [53] and  $^{208}\text{Pb}$  [54–56]. Recently,  $V_{\text{MU}} + \text{LS}$  was employed to study the medium-heavy nuclei around  $^{132}\text{Sn}$  and  $^{208}\text{Pb}$  [57, 58] in a unified way. Specifically, it has well reproduced the separation and excitation energies, as well as the nuclear level densities of nuclei with  $50 \leq Z \leq 56$  and  $80 \leq N \leq 84$  [59]. All the shell model calculations discussed here are performed with the code KSHELL [60].

In the case of  $^{142}\text{La}$ , the calculations are restricted to the condition that a maximum of two protons are allowed to occupy the  $\pi 1d_{3/2}$ ,  $\pi 0h_{11/2}$ , and  $\pi 2s_{1/2}$  orbital. In the

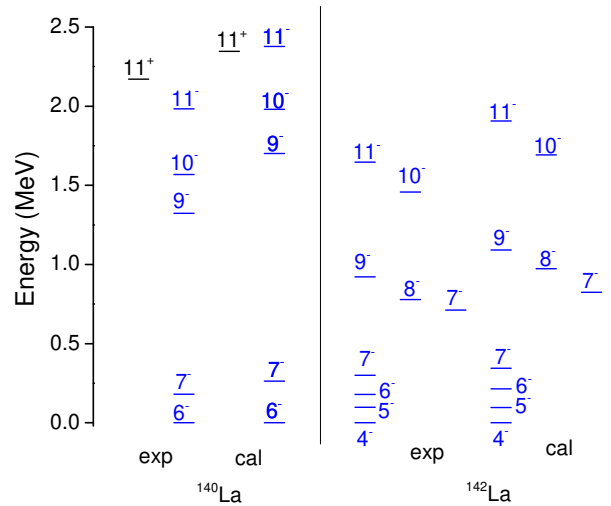


FIG. 17: Comparison of experimental energies (exp) of the excited states of even- $A$ ,  $^{140,142}\text{La}$  isotopes with the Shell Model calculations (cal). The positive and negative parity states are shown in black and blue colour respectively.

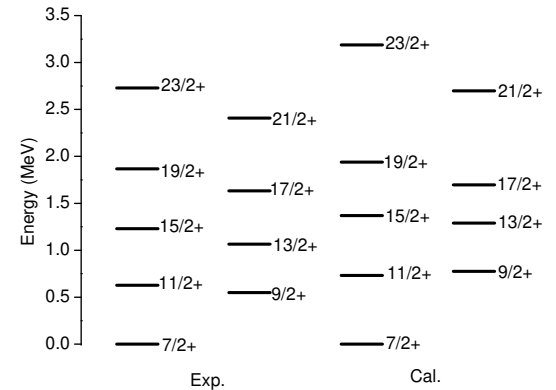


FIG. 18: Comparison of experimental energies (Exp.) of the excited states of  $^{141}\text{La}$  with Shell Model calculations (Cal.).

calculations for  $^{143}\text{La}$ , the restrictions for the proton excitation are the same as in  $^{142}\text{La}$ . Additionally, the number of neutrons particles in the  $\nu f_{7/2}$  orbital can range between two and four. These constraints for  $^{142,143}\text{La}$  arise from computational limitations due to the very large model space as the number of valence neutrons increases above  $N = 82$  closed shell. The calculated results for the excited states of even- $A$  La isotopes are compared with the corresponding experimental levels and are shown in Figs. 17. In this figure, only states lying above  $6^-$  and  $4^-$ , respectively, are shown, as the low-lying levels below  $6^-$  in  $^{140}\text{La}$  and below  $4^-$  in  $^{142}\text{La}$ , are not observed in the present work.

As can be seen from FIG. 17, the calculated excitation energies in  $^{140-142}\text{La}$  are consistent with the tentative assignment of spin and parity of the newly observed states. For the odd-odd nuclei  $^{140,142}\text{La}$ , the negative parity states can be divided into two groups based on

TABLE II: The two leading components of the Shell model configurations for  $^{140,142}\text{La}$ . The calculated excitation energies are shown in column Ex and are in MeV. The columns  $g7$ ,  $d5$ ,  $h11$ ,  $h9$ ,  $f7$ , and  $p3$  represent the occupancy in the  $\pi 0g_{7/2}$ ,  $\pi 1d_{5/2}$ ,  $\pi 0h_{11/2}$ ,  $\pi 0h_{9/2}$ ,  $\nu 1f_{7/2}$ , and  $\nu 2p_{3/2}$  orbitals, respectively. The last column shows the percentage of each configuration.

Nuclide	$J^\pi$	Ex	$g7$	$d5$	$h11$	$h9$	$f7$	$p3$	%
$^{140}\text{La}$	$2_1^-$	0	4	3	0	0	1	0	34
			6	1	0	0	1	0	17
	$2_2^-$	0.077	5	2	0	0	1	0	31
			3	4	0	0	1	0	13
	$6_1^-$	0.129	5	2	0	0	1	0	37
			3	4	0	0	1	0	11
	$4_1^-$	0.137	5	2	0	0	1	0	36
			3	4	0	0	1	0	12
	$3_1^-$	0.166	5	2	0	0	1	0	35
			3	4	0	0	1	0	11
	$1_1^-$	0.221	5	2	0	0	1	0	17
			6	1	0	0	1	0	15
	$5_1^-$	0.221	5	2	0	0	1	0	36
			3	4	0	0	1	0	10
	$0_1^-$	0.280	5	2	0	0	1	0	28
			3	4	0	0	1	0	19
	$7_1^-$	0.392	5	2	0	0	1	0	33
			3	4	0	0	1	0	14
	$8_1^-$	1.578	5	2	0	0	1	0	54
			3	4	0	0	1	0	7
	$9_1^-$	1.830	5	2	0	0	1	0	45
			3	4	0	0	1	0	12
	$8_1^+$	1.839	4	2	1	0	1	0	35
			6	0	1	0	1	0	22
	$10_1^-$	2.110	6	1	0	0	1	0	42
			4	3	0	0	1	0	29
	$11_1^+$	2.476	4	2	1	0	1	0	45
			6	0	1	0	1	0	15
	$11_1^-$	2.506	4	3	0	0	1	0	35
			6	1	0	0	1	0	33
$^{142}\text{La}$	$0_1^-$	0	4	3	0	0	3	0	13
			4	3	0	0	2	1	11
	$2_1^-$	0.180	4	3	0	0	3	0	17
			4	3	0	0	2	1	12
	$1_1^-$	0.254	4	3	0	0	3	0	19
			4	3	0	0	2	1	10
	$4_1^-$	0.387	4	3	0	0	3	0	14
			4	3	0	0	2	1	8
	$4_1^-$	0.417	4	3	0	0	3	0	10
			5	2	0	0	3	0	8
	$5_1^-$	0.484	3	4	0	0	3	0	10
			5	2	0	0	3	0	9
	$6_1^-$	0.601	5	2	0	0	3	0	15
			3	4	0	0	3	0	9
	$7_1^-$	0.731	3	4	0	0	3	0	16
			5	2	0	0	3	0	15
	$7_2^-$	1.211	4	3	0	0	3	0	19
			4	3	0	0	2	1	11
	$8_1^-$	1.361	4	3	0	0	3	0	14
			5	2	0	0	3	0	6
	$9_1^-$	1.479	3	4	0	0	3	0	17
			5	2	0	0	3	0	12
	$10_1^-$	2.080	4	3	0	0	3	0	20
			4	3	0	0	2	1	7
	$11_1^-$	2.294	3	4	0	0	3	0	20
			5	2	0	0	3	0	11

TABLE III: Same as in Table II, for  $^{141,143}\text{La}$ .

Nuclide	$J^\pi$	Ex	$g7$	$d5$	$h11$	$h9$	$f7$	$p3$	%
$^{141}\text{La}$	$7/2_1^+$	0	5	2	0	0	2	0	20
			3	4	0	0	2	0	11
	$11/2_1^+$	0.732	5	2	0	0	2	0	19
			3	4	0	0	2	0	11
	$9/2_1^+$	0.775	5	2	0	0	2	0	16
			5	2	0	0	1	1	7
	$13/2_1^+$	1.289	5	2	0	0	2	0	16
			3	4	0	0	2	0	7
	$15/2_1^+$	1.370	5	2	0	0	2	0	20
			3	4	0	0	2	0	11
	$17/2_1^+$	1.697	5	2	0	0	2	0	23
			3	4	0	0	2	0	12
	$19/2_1^+$	1.939	5	2	0	0	2	0	22
			3	4	0	0	2	0	16
	$21/2_1^+$	2.698	5	2	0	1	1	0	23
			3	2	2	1	1	0	10
	$23/2_1^+$	3.188	5	2	0	1	1	0	15
			3	4	0	1	1	0	8
$^{143}\text{La}$	$7/2_1^+$	0.	3	4	0	0	4	0	14
			5	2	0	0	4	0	7
	$5/2_1^+$	0.021	4	3	0	0	4	0	10
			3	4	0	0	4	0	8
	$3/2_1^+$	0.050	4	3	0	0	4	0	16
			4	3	0	0	3	1	7
	$5/2_2^+$	0.140	4	3	0	0	4	0	13
			3	4	0	0	4	0	5
	$7/2_1^+$	0.406	4	3	0	0	4	0	19
			4	3	0	0	3	1	11
	$11/2_1^+$	0.466	3	4	0	0	4	0	13
			3	4	0	0	3	1	6
	$9/2_1^+$	0.478	3	4	0	0	4	0	8
			4	3	0	0	4	0	7
	$5/2_3^+$	0.542	5	2	0	0	4	0	16
			5	2	0	0	3	1	6
	$7/2_3^+$	0.632	5	2	0	0	4	0	16
			3	4	0	0	4	0	7
	$9/2_2^+$	0.634	4	3	0	0	2	0	14
			3	4	0	0	3	1	7
	$9/2_3^+$	0.855	3	4	0	0	4	0	7
			5	2	0	0	4	0	7
	$11/2_2^+$	0.886	4	3	0	0	2	0	18
			4	3	0	0	3	1	11
	$13/2_1^+$	0.974	3	4	0	0	4	0	8
			3	4	0	0	3	1	8
	$15/2_1^+$	1.022	3	4	0	0	4	0	13
			3	4	0	0	3	1	8
	$11/2_3^+$	1.131	5	2	0	0	4	0	18
			3	4	0	0	3	1	7
	$13/2_1^-$	2.62	3	3	0	1	4	0	18
			3	2	0	1	2	0	16

their dominant shell model configurations. These configurations for the various states are given in Table II. For the lower group of states, including the  $6^-$ ,  $7^-$ , and  $9^-$  states in  $^{140}\text{La}$  and the  $5^-$ ,  $6^-$ ,  $7_1^-$ , and  $9_1^-$  states in  $^{142}\text{La}$ , are dominated by the  $\pi(0g_{7/2})^5(1d_{5/2})^2\nu(1f_{7/2})^n$  and  $\pi(0g_{7/2})^3(1d_{5/2})^4\nu(1f_{7/2})^n$  configuration, with  $n$

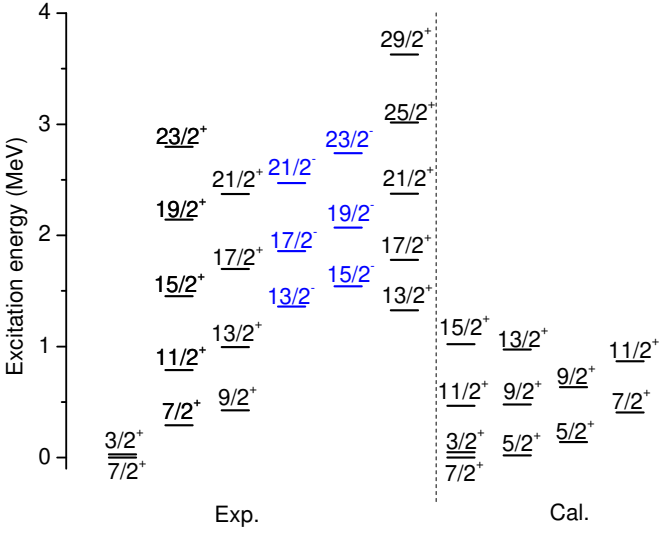


FIG. 19: Comparison of experimental energies (Exp.) of the excited states of  $^{143}\text{La}$  with Shell Model calculations (Cal.).

representing the valence neutron number. For the others, the  $4^-$ ,  $10^-$ , and  $11^-$  states in  $^{140}\text{La}$  are dominated by the  $\pi(0g_{7/2})^4(1d_{5/2})^3\nu(1f_{7/2})$  and the  $\pi(0g_{7/2})^6(1d_{5/2})\nu(1f_{7/2})$  configurations, while the  $\pi(0g_{7/2})^4(1d_{5/2})^3\nu(1f_{7/2})^3$  is the leading component in the  $7_2^-$ ,  $8^-$ , and  $10^-$  states in  $^{142}\text{La}$ . Overall, the dominant configurations represent a larger fraction in  $^{140}\text{La}$  as compared to  $^{142}\text{La}$ , reflecting an increase in collectivity with increasing number of valence neutrons. Regarding the positive parity states in  $^{140}\text{La}$ , the  $8^+$  and  $11^+$  states are dominated ( $\approx 40\%$ ) by the  $\pi(0g_{7/2})^4(1d_{5/2})^2(0h_{11/2})\nu(1f_{7/2})$  configuration. However, only the  $11^+$  state is tentatively identified in the present experiment, while the  $8^+$  state could not be observed.

For  $^{141}\text{La}$ , the calculated energies align fairly well with the observed levels as shown in FIG. 18. This agreement is expected, given that single-particle character tends to be more pronounced in odd- $A$  nuclei than in odd-odd nuclei. Shell model configurations for various states in  $^{141-143}\text{La}$  are given in Table III. The most probable configuration of the first  $7/2^+$ ,  $9/2^+$ ,  $11/2^+$ ,  $13/2^+$ ,  $15/2^+$ ,  $17/2^+$ , and  $19/2^+$  states is  $\pi(0g_{7/2})^5(1d_{5/2})^2\nu(1f_{7/2})^2$ . On this basis, the  $21/2^+$  and  $23/2^+$  states result from a particle-hole excitation from  $\nu 1f_{7/2}$  to  $\nu 1f_{5/2}$ . The intermediate values of the fraction of dominant contribution can be seen to lie between those for  $^{140}\text{La}$  and  $^{142}\text{La}$ . The new band built on the 1218 keV state in  $^{141}\text{La}$  has not been predicted in the present shell-model calculation. As mentioned earlier in the case of  $^{143}\text{La}$ , the restricted large valence space and very large computing time do not allow for a comparison of all of the measured states. The major contributions only for a few low-lying states are shown in Table III. A comparison with the shell model calculations for a restricted number of states for  $^{143}\text{La}$  is

shown in Fig. 19.

## B. Possible octupole deformation in $^{143}\text{La}$

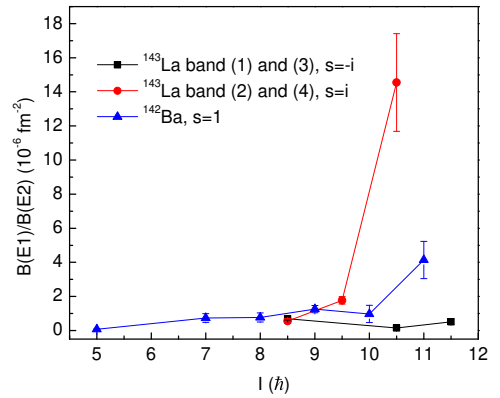


FIG. 20:  $B(E1)/B(E2)$  ratios of the  $s = \pm i$  band structures (namely Bands (1), (3) and Bands (2), (4)) in  $^{143}\text{La}$ .

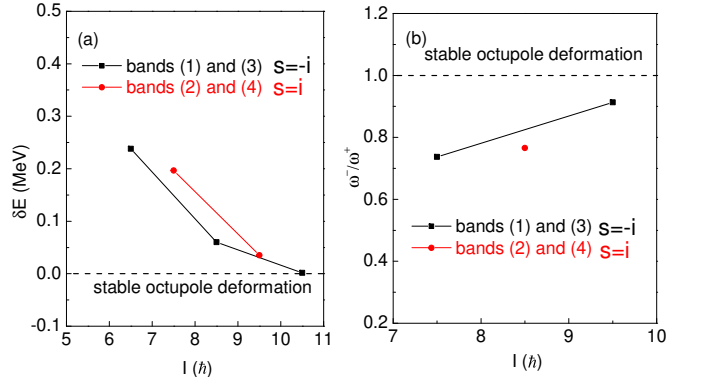


FIG. 21: The energy displacement  $\delta E$  (a) and the rotational frequency ratio  $\omega^-/\omega^+$  (b) of the  $s = \pm i$  band structures (namely, Bands (2), (4) and (1), (3)) in  $^{143}\text{La}$ .

As the high spin level structure of  $^{143}\text{La}$  shows pairs of opposite parity bands, with connecting  $E1$  transitions between the two, the excited structures of  $^{143}\text{La}$  are further discussed in the context of the possible presence of reflection asymmetric shape resulting in octupole deformation.

Bands (1) and (3) in  $^{143}\text{La}$  were assigned as  $s = i$  octupole doublet by Ref. [25] with a  $5/2^+$  band-head. With the new assignment of the band-head from the current work, these two bands should now form the  $s = -i$  octupole doublet, as the spins of the levels of the two bands increment by  $1\hbar$  in the new assignments. The negative parity Band (3) (labeled as Band (1) in Ref. [25]) was interpreted as the single particle levels coupling to the  $1^-$  and  $3^-$  levels in the  $^{142}\text{Ba}$  core [25]. Taking this interpretation to Bands (2) and (4), Band (4) can form the negative-parity part of the  $s = i$  doublet with Band

(2). It should be noted that multiple octupole doublets in a single nucleus have been seen only in limited cases. Recently, three octupole doublets were reported in the neighboring  $^{145}\text{Ba}$  nucleus [14].

Energy displacement  $\delta E$  between the opposite parity states of the same spin and rotational frequency ratios  $\omega^\mp/\omega^\pm$  are quantities to evaluate the stability of octupole deformation [18]. These quantities are calculated as follows:

$$\delta E(I) = E(I) \mp -\frac{E(I+1)^\pm - E(I-1)^\pm}{2} \quad (1)$$

$$\frac{\omega(I)^\mp}{\omega(I)^\pm} = 2 \times \frac{E(I+1)^\mp - E(I-1)^\mp}{E(I+2)^\pm - E(I-2)^\pm} \quad (2)$$

$B(\text{E}1)/B(\text{E}2)$  ratios of the octupole doublet are another such an observable.

We first look at the  $B(\text{E}1)/B(\text{E}2)$  ratios of the the octupole doublet. The  $B(\text{E}1)/B(\text{E}2)$  ratios of the the octupole doublet with simplex quantum number  $s = \pm i$  are extracted from the measured intensities of  $\gamma$  rays and are depicted in FIG. 20. The ratios of the new  $s = i$  band structures show an increasing trend with spin and have a much larger value at higher spin. The reason for this is unclear and could be related to additional uncertainties in the extracted intensities beyond the fitting errors. The sharply increasing  $B(\text{E}1)/B(\text{E}2)$  ratios for the  $s = i$  structure were also reported in  $^{143}\text{Ba}$ , with large staggering at higher spins [14]. The current data on  $^{143}\text{La}$  do not extend to spins high enough to investigate such phenomena.

The energy displacement  $\delta E$  and rotational frequency ratios  $\omega^\mp/\omega^\pm$  between the opposite parity states of the same spin, deduced from the current study are depicted in FIG. 21(a) and (b) respectively. For stabilized octupole shape, the expected values are  $\delta E = 0$  and  $\omega^\mp/\omega^\pm = 1$ , which are shown as dotted lines in the respective plots. It can be seen from FIG. 21(a) that the  $\delta E$  values for  $s = \pm i$  doublets both decrease sharply with increasing spin and reach the stable octupole limit at high spin. The variation of  $\delta E$  does not show any dependence on the simplex quantum number within the observed spin range, which is expected in the case of stabilized octupole deformation. A similar decreasing trend was observed in the case of  $N = 86$  isotones of Ba ( $^{142}\text{Ba}$ ) and Ce ( $^{144}\text{Ce}$ ) [25]. Furthermore, the  $^{144}\text{Ce}$  nucleus reaches the stable limit at spin 7, while  $^{142}\text{Ba}$  does not reach the stable limit.

Indication about the nature of octupole excitation can also be obtained from the quantity  $\omega^\mp/\omega^\pm = 1$ , i.e. the rotational frequency ratio of the opposite parity bands. As can be seen from FIG. 21(b), the rotational frequency ratio approaches unity (the limit corresponding to stable octupole deformation) for higher spins for the  $s = -i$  structure. The limited data for the  $s = i$  structure did not allow us to obtain the nature of its variation with

spin. The behaviour of the parity doublet bands in  $^{143}\text{La}$  is found to be similar to that in  $^{142}\text{Ba}$  [12]. Thus the various observables presented in this work, indicate the presence of stable octupole deformation at high spins in  $^{143}\text{La}$ .

## V. SUMMARY

The high spin states in  $^{140-142}\text{La}$  have been reported for the first time. The previous assignments of transitions and levels in  $^{142}\text{La}$  reported in literature, are now assigned to  $^{143}\text{La}$  from direct (A,Z) identification. The present results could be obtained, thanks to two powerful complementary measurements of high-fold gamma rays from Cf fission and  $\gamma$  rays in coincidence with isotopically identified fission fragments produced in fission of  $^{238}\text{U} + ^9\text{Be}$  system around the barrier. The level structures are interpreted in terms of the systematics of neighbouring odd-Z nuclei above  $Z = 50$  shell closure and large-scale shell model calculations. The present measurement for  $^{140-143}\text{La}$  isotopes provides the missing information for understanding the evolution of the excitation modes in the La isotopic chain above the  $N = 82$  shell closure. Based on the present work, the presence of a pair of parity doublet band structures is established in  $^{143}\text{La}$ , not routinely observed in many nuclei. The properties of these parity doublet band structures indicate the presence of stable octupole deformation in  $^{143}\text{La}$ . Based on the known structures of the larger-N La isotopes, the octupole deformation is observed to decrease while going towards the normally expected region of octupole collectivity near  $N \approx 90$  unlike in nearby isotopes. Further Potential Energy Surface (PES) / Total Routhian Surface (TRS) / Cranked Shell Model (CSM) calculations or microscopic shell model calculations using a larger model space could give a greater insight into this behaviour in the La isotopes. Separation energies obtained from new precision mass measurement [27] have shown the strongest change of two-neutron separation energy in the periodic table between  $N = 92$  and  $N = 94$  in La. This motivates a deeper investigation of the level structure of nuclei like  $^{153}\text{La}$ .

## VI. ACKNOWLEDGEMENTS

The authors gratefully acknowledge the AGATA collaboration for the availability of the AGATA  $\gamma$  tracking array at GANIL. We would like to thank the GANIL accelerator staff for their technical contributions. We thank A. O. Macchiavelli for help in data collection during the experiment. SB, SB and RB acknowledge the support received from CEFIPRA project No. 5604-4 and SB, RP acknowledge the support from the LIA France-India agreement. PB and AM acknowledge support from the Polish National Science Centre (NCN) under Contract No. 2016/22/M/ST2/00269 and the French

LEA COPIGAL project. HLC and PF acknowledge support from the U.S. Department of Energy, Office of Science, Office of Nuclear Physics under Contract No. DE-AC02-05CH11231 (LBNL). RMPV acknowledges partial support from the Ministry of Science, Spain, under the grants BES-2012-061407, SEV-2014-0398, FPA2017-84756-C4 and from EU FEDER funds. The work at Van-

derbilt University and Lawrence Berkeley National Laboratory are supported by the U.S. Department of Energy under Grant No. DE-FG05-88ER40407 and Contract No. DE-AC03-76SF00098. EW also acknowledges support from Shandong Provincial Outstanding Young Scholars Fund (Overseas) Program No. 2025HWYQ-028 and Shandong University Qilu Young Scholar.

---

[1] P. A. Butler and W. Nazarewicz, *Reviews of Modern Physics* **68**, 349 (1996).

[2] I. Ahmad and P. A. Butler, *Ann. Rev. of Nucl. Part. Sc.* **43**, 71 (1993).

[3] L. P. Gaffney, P. A. Butler, M. Scheck, A. B. Hayes, F. Wenander, M. Albers, B. Bastin, C. Bauer, A. Blazhev, S. Bonig, N. Bree, J. Cederkall, T. Chupp, D. Cline, T. E. Cocolios, T. Davinson, H. De Witte, J. Diriken, T. Grahn, A. Herzan, M. Huyse, D. G. Jenkins, D. T. Joss, N. Kesteloot, J. Konki, M. Kowalczyk, T. Kröll, E. Kwan, R. Lutter, K. Moschner, P. Napiorkowski, J. Pakarinen, M. Pfeiffer, D. Radeck, P. Reiter, K. Reynders, S. V. Rigby, L. M. Robledo, M. Rudigier, S. Sambi, M. Seidlitz, B. Siebeck, T. Stora, P. Thoele, P. Van Duppen, M. J. Vermeulen, M. von Schmid, D. Voulot, N. Warr, K. Wimmer, K. Wrzosek-Lipska, C. Y. Wu, and M. Zielińska, *Nature* **497**, 199 (2013).

[4] S. J. Zhu, M. Sakhaei, J. H. Hamilton, A. V. Ramayya, N. T. Brewer, J. K. Hwang, S. H. Liu, E. Y. Yeoh, Z. G. Xiao, Q. Xu, Z. Zhang, Y. X. Luo, J. O. Rasmussen, I. Y. Lee, K. Li, and W. C. Ma, *Phys. Rev. C* **85**, 014330 (2012).

[5] H. J. Li, S. J. Zhu, J. H. Hamilton, A. V. Ramayya, J. K. Hwang, Z. G. Xiao, M. Sakhaei, J. Y. Guo, S. W. Chen, N. T. Brewer, S. H. Liu, K. Li, E. Y. Yeoh, Z. Zhang, Y. X. Luo, J. O. Rasmussen, I. Y. Lee, G. Ter-Akopian, A. Daniel, Y. T. Oganessian, and W. C. Ma, *Phys. Rev. C* **86**, 067302 (2012).

[6] E. H. Wang, A. Lemasson, J. H. Hamilton, A. V. Ramayya, J. K. Hwang, J. M. Eldridge, A. Navin, M. Rejmund, S. Bhattacharyya, S. H. Liu, N. T. Brewer, Y. X. Luo, J. O. Rasmussen, H. L. Liu, H. Zhou, Y. X. Liu, H. J. Li, Y. Sun, F. R. Xu, S. J. Zhu, G. M. Ter-Akopian, Y. T. Oganessian, M. Caamaño, E. Clément, O. Delaune, F. Farget, G. de France, and B. Jacquot, *Phys. Rev. C* **92**, 034317 (2015).

[7] W. Urban, K. Sieja, T. Rząca-Urban, M. Czerwiński, H. Naiđja, F. Nowacki, A. G. Smith, and I. Ahmad, *Phys. Rev. C* **93**, 034326 (2016).

[8] Y. Huang, S. J. Zhu, J. H. Hamilton, E. H. Wang, A. V. Ramayya, Z. G. Xiao, H. J. Li, Y. X. Luo, J. O. Rasmussen, G. M. Ter-Akopian, and Y. T. Oganessian, *Phys. Rev. C* **93**, 064321 (2016).

[9] S. J. Zhu, E. H. Wang, J. H. Hamilton, A. V. Ramayya, Y. X. Liu, N. T. Brewer, Y. X. Luo, J. O. Rasmussen, Z. G. Xiao, Y. Huang, G. M. Ter-Akopian, and T. Oganessian, *Phys. Rev. Lett.* **124**, 032501 (2020).

[10] T. Rząca-Urban, W. Urban, J. A. Pinston, G. S. Simpson, A. G. Smith, and I. Ahmad, *Phys. Rev. C* **86**, 044324 (2012).

[11] Y. Huang, S. J. Zhu, J. H. Hamilton, Y. J. Chen, E. H. Wang, A. V. Ramayya, Z. G. Xiao, H. J. Li, Y. X. Luo, J. O. Rasmussen, G. M. Ter-Akopian, and Y. T. Oganessian, *Journal of Physics G: Nuclear and Particle Physics* **44**, 095101 (2017).

[12] Y. Luo, J. Rasmussen, J. Hamilton, A. Ramayya, S. Liu, E. Jones, P. Gore, C. Goodin, N. Stone, S. Zhu, J. Hwang, K. Li, H. Crowell, I. Lee, G. Ter-Akopian, A. Daniel, M. Stoyer, R. Donangelo, W. Ma, and J. Cole, *Nuclear Physics A* **838**, 1 (2010).

[13] E. H. Wang, W. Lewis, C. J. Zachary, J. H. Hamilton, A. V. Ramayya, J. K. Hwang, S. H. Liu, N. T. Brewer, Y. X. Luo, J. O. Rasmussen, S. J. Zhu, G. M. Ter-Akopian, and Y. T. Oganessian, *The European Physical Journal A* **53**, 234 (2017).

[14] N. Brewer, E. Wang, W. Yzaguirre, J. Hamilton, K. Nomura, A. Ramayya, S. Liu, J. Hwang, B. Musangu, J. Eldridge, C. Zachary, Y. Luo, J. Rasmussen, S. Zhu, C. Goodin, G. Ter-Akopian, A. Daniel, and Y. Oganessian, *Nuclear Physics A* **1039**, 122738 (2023).

[15] E. Wang, N. Brewer, J. Hamilton, A. Ramayya, W. Yzaguirre, J. Hwang, S. Liu, Y. Luo, J. Rasmussen, S. Zhu, G. Ter-Akopian, and Y. Oganessian, *Nuclear Physics A* **1015**, 122281 (2021).

[16] T. Rząca-Urban, W. Urban, J. A. Pinston, G. S. Simpson, A. G. Smith, and I. Ahmad, *Phys. Rev. C* **86**, 044324 (2012).

[17] G. Leander, W. Nazarewicz, P. Olanders, I. Ragnarsson, and J. Dudek, *Physics Letters B* **152**, 284 (1985).

[18] W. Nazarewicz and P. Olanders, *Nuclear Physics A* **441**, 420 (1985).

[19] A. V. Afanasev and I. Ragnarsson, *Phys. Rev. C* **51**, 1259 (1995).

[20] Y. J. Chen, S. J. Zhu, J. H. Hamilton, A. V. Ramayya, J. K. Hwang, M. Sakhaei, Y. X. Luo, J. O. Rasmussen, K. Li, I. Y. Lee, X. L. Che, H. B. Ding, and M. L. Li, *Phys. Rev. C* **73**, 054316 (2006).

[21] S. J. Zhu, J. H. Hamilton, A. V. Ramayya, M. G. Wang, J. K. Hwang, E. F. Jones, L. K. Peker, B. R. S. Babu, G. Drafta, W. C. Ma, G. L. Long, L. Y. Zhu, M. Li, C. Y. Gan, T. N. Ginter, J. Kormicki, J. K. Deng, D. T. Shi, W. E. Collins, J. D. Cole, R. Aryaeinejad, M. W. Drigert, J. O. Rasmussen, R. Donangelo, J. Gilat, S. Asztalos, I. Y. Lee, A. O. Macchiavelli, S. Y. Chu, K. E. Gregorich, M. F. Mohar, M. A. Stoyer, R. W. Lougheed, K. J. Moody, J. F. Wild, S. G. Prussin, G. M. Ter-Akopian, A. V. Daniel, and Y. T. Oganessian, *Phys. Rev. C* **59**, 1316 (1999).

[22] S. Chakraborty, H. Sharma, S. Tiwary, C. Majumder, A. Gupta, P. Banerjee, S. Ganguly, S. Rai, Pragati, Mayank, S. Kumar, A. Kumar, R. Palit, S. Bhattacharjee, R. Singh, and S. Muralithar, *Nuclear Physics A* **1037**, 122706 (2023).

[23] W. Nazarewicz, P. Olanders, I. Ragnarsson,

J. Dudek, G. Leander, P. Möller, and E. Ruchowsa, *Nuclear Physics A* **429**, 269 (1984).

[24] R. Piepenbring, *Zeitschrift für Physik A Atoms and Nuclei* **322**, 495 (1985).

[25] Y. Luo, J. Hamilton, J. Rasmussen, A. Ramayya, C. Goodin, S. Zhu, J. Hwang, K. Li, D. Fong, I. Stefanescu, I. Lee, G. Ter-Akopian, A. Daniel, M. Stoyer, R. Donangelo, W. Ma, and J. Cole, *Nuclear Physics A* **818**, 121 (2009).

[26] W. Urban, W. R. Phillips, J. L. Durell, M. A. Jones, M. Leddy, C. J. Pearson, A. G. Smith, B. J. Varley, I. Ahmad, L. R. Morss, M. Bentaleb, E. Lubkiewicz, and N. Schulz, *Phys. Rev. C* **54**, 945 (1996).

[27] A. Jaries, M. Stryjczyk, A. Kankainen, T. Eronen, O. Beliuskina, T. Dickel, M. Flayol, Z. Ge, M. Hukkanen, M. Mugeot, S. Nikas, I. Pohjalainen, A. Raggio, M. Reponen, J. Ruotsalainen, and V. Virtanen, *Phys. Rev. Lett.* **134**, 042501 (2025).

[28] Y. X. Luo *et al.*, *Int. J. Mod. Phys. E* **30**, 2150037 (2021).

[29] S. Bhattacharyya, E. H. Wang, A. Navin, M. Rejmund, J. H. Hamilton, A. V. Ramayya, J. K. Hwang, A. Lemasson, A. V. Afanasjev, S. Bhattacharya, J. Ranger, M. Caamaño, E. Clément, O. Delaune, F. Farget, G. de France, B. Jacquot, Y. X. Luo, Y. T. Oganessian, J. O. Rasmussen, G. M. Ter-Akopian, and S. J. Zhu, *Phys. Rev. C* **98**, 044316 (2018).

[30] E. H. Wang, J. H. Hamilton, A. V. Ramayya, C. J. Zachary, A. Lemasson, A. Navin, M. Rejmund, S. Bhattacharyya, Q. B. Chen, S. Q. Zhang, J. M. Eldridge, J. K. Hwang, N. T. Brewer, Y. X. Luo, J. O. Rasmussen, S. J. Zhu, G. M. Ter-Akopian, Y. T. Oganessian, M. Caamaño, E. Clément, O. Delaune, F. Farget, G. de France, and B. Jacquot, *Phys. Rev. C* **103**, 034301 (2021).

[31] M. Rejmund, B. Lecornu, A. Navin, C. Schmitt, S. Damoy, O. Delaune, J. M. Enguerrand, G. Fremont, P. Gangnat, L. Gaudefroy, B. Jacquot, J. Pancin, S. Pullanhiotan, and C. Spitaels, *Nucl. Instr. Meth. Phys. Res. A* **646**, 184 (2011).

[32] A. Navin and M. Rejmund, in *McGraw-Hill Yearbook of Science and Technology* (2014) p. 137.

[33] Y. H. Kim, A. Lemasson, M. Rejmund, A. Navin, S. Biswas, C. Michelagnoli, I. Stefan, R. Banik, P. Bednarczyk, S. Bhattacharyya, S. Bhattacharyya, E. Clément, H. L. Crawford, G. De France, P. Fallon, J. Goupil, B. Jacquot, H. J. Li, J. Ljungvall, A. O. Macchiavelli, A. Maj, L. Ménager, V. Morel, R. Palit, R. M. Pérez-Vidal, J. Ropert, and C. Schmitt, *Eur. Phys. J. A* **53**, 162 (2017).

[34] M. Vandebrouck, A. Lemasson, M. Rejmund, G. Fremont, J. Pancin, A. Navin, C. Michelagnoli, J. Goupil, C. Spitaels, and B. Jacquot, *Nucl. Instr. Meth. Phys. Res. A* **812**, 112 (2016).

[35] E. Clément *et al.*, *Nucl. Instr. Meth. Phys. Res. A* **855**, 1 (2017).

[36] R. Banik, S. Bhattacharyya, M. Rejmund, A. Lemasson, S. Biswas, A. Navin, Y. H. Kim, C. Michelagnoli, I. Stefan, P. Bednarczyk, S. Bhattacharyya, E. Clément, H. L. Crawford, G. de France, P. Fallon, G. Fremont, J. Goupil, B. Jacquot, H. J. Li, J. Ljungvall, A. Maj, L. Ménager, V. Morel, G. Mukherjee, R. Palit, R. M. Pérez-Vidal, J. Ropert, and C. Schmitt, *Phys. Rev. C* **102**, 044329 (2020).

[37] D. Radford, *Nucl. Instr. Meth. Phys. Res. A* **361**, 297 (1995).

[38] R. A. Meyer, K. V. Marsh, H. Seyfarth, S. Brant, M. Bogdanović, and V. Paar, *Phys. Rev. C* **41**, 1172 (1990).

[39] J. Rufino, E. A. McCutchan, S. Zhu, A. A. Sonzogni, M. Alcorta, P. F. Bertone, M. P. Carpenter, J. Clark, C. R. Hoffman, R. V. F. Janssens, F. G. Kondev, T. Lauritsen, C. J. Lister, R. Pardo, A. Rogers, G. Savard, D. Seweryniak, and R. Vondrasek, *Phys. Rev. C* **106**, 034318 (2022).

[40] C. Chung, W. B. Walters, D. S. Brenner, A. Aprahamian, R. L. Gill, M. Shmid, R. E. Chrien, L. J. Yuan, A. Wolf, and Z. Berant, *Phys. Rev. C* **28**, 2099 (1983).

[41] E. T. Journey, R. K. Sheline, E. B. Shera, H. R. Koch, B. P. K. Maier, U. Gruber, H. Baader, D. Breitig, O. W. B. Schult, J. Kern, and G. L. Struble, *Phys. Rev. C* **2**, 2323 (1970).

[42] J. G. Wang, S. J. Zhu, J. H. Hamilton, A. V. Ramayya, J. K. Hwang, Y. X. Luo, Y. J. Chen, J. O. Rasmussen, I. Y. Lee, X. L. Che, H. B. Ding, K. Li, C. T. Goodin, and Q. Xu, *Phys. Rev. C* **75**, 064301 (2007).

[43] J. Kern, G. L. Struble, and R. K. Sheline, *Phys. Rev. C* **153**, 1331 (1966).

[44] S. H. Liu, J. H. Hamilton, A. V. Ramayya, A. Covello, A. Gargano, N. Itaco, N. J. Stone, A. V. Daniel, J. K. Hwang, Y. X. Luo, J. O. Rasmussen, G. M. Ter-Akopian, S. J. Zhu, and W. C. Ma, *Phys. Rev. C* **81**, 014316 (2010).

[45] S. H. Faller, C. A. Stone, J. D. Robertson, C. Chung, N. K. Aras, and W. B. Walters, *Phys. Rev. C* **34**, 654 (1986).

[46] S. H. Liu, J. H. Hamilton, A. V. Ramayya, A. Covello, A. Gargano, N. Itaco, Y. X. Luo, J. O. Rasmussen, J. K. Hwang, A. V. Daniel, G. M. Ter-Akopian, S. J. Zhu, and W. C. Ma, *Phys. Rev. C* **80**, 044314 (2009).

[47] S. H. Faller, J. D. Robertson, E. M. Baum, C. Chung, C. A. Stone, and W. B. Walters, *Phys. Rev. C* **38**, 307 (1988).

[48] T. Otsuka, T. Suzuki, M. Honma, Y. Utsuno, N. Tsunoda, K. Tsukiyama, and M. Hjorth-Jensen, *Phys. Rev. Lett.* **104**, 012501 (2010).

[49] G. Bertsch, J. Borysowicz, H. McManus, and W. G. Love, *Nucl. Phys. A* **284**, 399 (1977).

[50] C. Yuan, T. Suzuki, T. Otsuka, F. Xu, and N. Tsunoda, *Phys. Rev. C* **85**, 064324 (2012).

[51] Y. Utsuno, T. Otsuka, B. A. Brown, M. Honma, T. Mizusaki, and N. Shimizu, *Phys. Rev. C* **86**, 051301(R) (2012).

[52] T. Togashi, N. Shimizu, Y. Utsuno, T. Otsuka, and M. Honma, *Phys. Rev. C* **91**, 024320 (2015).

[53] C. Yuan, Z. Liu, F. Xu, P. Walker, Z. Podolyak, C. xu, Z. Ren, B. Ding, M. Liu, X. Liu, H. Xu, X. Zhou, Y. Zhang, and W. Zuo, *Phys. Lett. B* **762**, 237 (2016).

[54] C. Yuan, M. Liu, N. Shimizu, Z. Podolyák, T. Suzuki, T. Otsuka, and Z. Liu, *Phys. Rev. C* **106**, 044314 (2022).

[55] Z. Y. Zhang, H. B. Yang, M. H. Huang, Z. G. Gan, C. X. Yuan, C. Qi, A. N. Andreyev, M. L. Liu, L. Ma, M. M. Zhang, Y. L. Tian, Y. S. Wang, J. G. Wang, C. L. Yang, G. S. Li, Y. H. Qiang, W. Q. Yang, R. F. Chen, H. B. Zhang, Z. W. Lu, X. X. Xu, L. M. Duan, H. R. Yang, W. X. Huang, Z. Liu, X. H. Zhou, Y. H. Zhang, H. S. Xu, N. Wang, H. B. Zhou, X. J. Wen, S. Huang, W. Hua, L. Zhu, X. Wang, Y. C. Mao, X. T. He, S. Y. Wang, W. Z. Xu, H. W. Li, Z. Z. Ren, and S. G. Zhou, *Phys. Rev. Lett.* **126**, 152502 (2021).

[56] H. B. Yang, Z. G. Gan, Z. Y. Zhang, M. H. Huang, L. Ma, M. M. Zhang, C. X. Yuan, Y. F. Niu, C. L. Yang, Y. L. Tian, L. Guo, Y. S. Wang, J. G. Wang, H. B. Zhou, X. J. Wen, H. R. Yang, X. H. Zhou, Y. H. Zhang, W. X. Huang, Z. Liu, S. G. Zhou, Z. Z. Ren, H. S. Xu, V. K. Utyonkov, A. A. Voinov, Y. S. Tsyganov, A. N. Polyakov, and D. I. Solovyev, *Phys. Rev. C* **105**, L051302 (2022).

[57] C. X. Yuan, Y. L. Ge, M. L. Liu, G. S. Chen, and B. S. Cai, *EPJ Web of Conf.* **239**, 04002 (2020).

[58] M. Liu and C. Yuan, *Int. J. Mod. Phys. E* **32**, 2330003 (2023).

[59] J. Chen, M. Liu, C. Yuan, S. Chen, N. Shimizu, X. Sun, R. Xu, and Y. Tian, *Phys. Rev. C* **107**, 054306 (2023).

[60] N. Shimizu, T. Mizusaki, Y. Utsuno, and Y. Tsunoda, *Comput. Phys. Commun.* **244**, 372 (2019).

### Appendix A: Tables of Transition Energies and Intensities

This is the beginning of appendix.

TABLE I: The energies ( $E_\gamma$ ) and relative intensities ( $I_\gamma$ ) of the  $\gamma$  rays assigned to  $^{140}\text{La}$  isotopes along with the spin and parity of the initial ( $J_i^\pi$ ) and the final ( $J_f^\pi$ ) states and the energy of the initial state ( $E_i$ ).

$E_\gamma$ (keV)	$E_i$ (keV)	$J_i^\pi \rightarrow J_f^\pi$	$I_\gamma$ (Err.)
181	230	(7 <sup>-</sup> ) $\rightarrow$ 6 <sup>-</sup>	95 (10)
211	260	— $\rightarrow$ 6 <sup>-</sup>	36 (5)
236	285	(7 <sup>-</sup> ) $\rightarrow$ 6 <sup>-</sup>	98 (12)
245	1617	(10 <sup>-</sup> ) $\rightarrow$ (9 <sup>-</sup> )	100 (11)
416	2033	(11 <sup>-</sup> ) $\rightarrow$ (10 <sup>-</sup> )	57 (5)
603	2220	(11 <sup>+</sup> ) $\rightarrow$ (10 <sup>-</sup> )	53 (6)
724	—	— $\rightarrow$ —	34 (5)
1141	1372	(9 <sup>-</sup> ) $\rightarrow$ (7 <sup>-</sup> )	87 (10)
1223	1508	(9 <sup>-</sup> ) $\rightarrow$ (7 <sup>-</sup> )	25 (4)
1262	1522	— $\rightarrow$ —	26 (5)

TABLE II: The energies ( $E_\gamma$ ) and relative intensities ( $I_\gamma$ ) of the  $\gamma$  rays assigned to  $^{141}\text{La}$  isotopes along with the spin and parity of the initial ( $J_i^\pi$ ) and the final ( $J_f^\pi$ ) states and the energy of the initial state ( $E_i$ ).

$E_\gamma$ (keV)	$E_i$ (keV)	$J_i^\pi \rightarrow J_f^\pi$	$I_\gamma$ (Err.)
163	1230	(15/2 <sup>+</sup> ) $\rightarrow$ (13/2 <sup>+</sup> )	21 (2)
189	—	— $\rightarrow$ —	9 (1)
234	1867	(19/2 <sup>+</sup> ) $\rightarrow$ (17/2 <sup>+</sup> )	11 (2)
320	2729	(23/2 <sup>+</sup> ) $\rightarrow$ (21/2 <sup>+</sup> )	4 (1)
403	1633	(17/2 <sup>+</sup> ) $\rightarrow$ (15/2 <sup>+</sup> )	21 (3)
410	2278	— $\rightarrow$ (19/2 <sup>+</sup> )	10 (2)
416	2694	— $\rightarrow$ —	30 (3)
439	1067	(13/2 <sup>+</sup> ) $\rightarrow$ (11/2 <sup>+</sup> )	19 (2)
511	2278	— $\rightarrow$ —	31 (4)
517	1067	(13/2 <sup>+</sup> ) $\rightarrow$ (9/2 <sup>+</sup> )	26 (3)
537	1767	— $\rightarrow$ (15/2 <sup>+</sup> )	—
549	1767	— $\rightarrow$ —	27 (7)
551	551	(9/2 <sup>+</sup> ) $\rightarrow$ (7/2 <sup>+</sup> )	34 (7)
566	1633	(17/2 <sup>+</sup> ) $\rightarrow$ (13/2 <sup>+</sup> )	17 (1)
590	1218	— $\rightarrow$ (11/2 <sup>+</sup> )	29 (3)
602	1230	(15/2 <sup>+</sup> ) $\rightarrow$ (11/2 <sup>+</sup> )	60 (6)

628	628	(11/2 <sup>+</sup> ) $\rightarrow$ (7/2 <sup>+</sup> )	100 (11)
637	1867	(19/2 <sup>+</sup> ) $\rightarrow$ (15/2 <sup>+</sup> )	21 (3)
776	2409	(21/2 <sup>+</sup> ) $\rightarrow$ (17/2 <sup>+</sup> )	23 (3)
862	2729	(23/2 <sup>+</sup> ) $\rightarrow$ (19/2 <sup>+</sup> )	14 (2)
957	3650	— $\rightarrow$ —	12 (2)

TABLE III: The energies ( $E_\gamma$ ) and relative intensities ( $I_\gamma$ ) of the  $\gamma$  rays assigned to  $^{142}\text{La}$  isotopes along with the spin and parity of the initial ( $J_i^\pi$ ) and the final ( $J_f^\pi$ ) states and the energy of the initial state ( $E_i$ ).

$E_\gamma$ (keV)	$E_i$ (keV)	$J_i^\pi \rightarrow J_f^\pi$	$I_\gamma$ (Err.)
82	326	(6 <sup>-</sup> ) $\rightarrow$ (5 <sup>-</sup> )	64 (7)
98	244	(5 <sup>-</sup> ) $\rightarrow$ (4 <sup>-</sup> )	100 (14)
120	446	(7 <sup>-</sup> ) $\rightarrow$ (6 <sup>-</sup> )	64 (9)
163	—	— $\rightarrow$ —	13 (2)
210	—	— $\rightarrow$ —	8 (1)
269	—	— $\rightarrow$ —	12 (2)
463	—	— $\rightarrow$ —	12 (2)
502	—	— $\rightarrow$ —	43 (5)
532	858	(7 <sup>-</sup> ) $\rightarrow$ (6 <sup>-</sup> )	21 (3)
550	—	— $\rightarrow$ —	23 (3)
562	—	— $\rightarrow$ —	21 (3)
600	925	(8 <sup>-</sup> ) $\rightarrow$ (6 <sup>-</sup> )	50 (5)
614	858	(7 <sup>-</sup> ) $\rightarrow$ (5 <sup>-</sup> )	21 (3)
622	1068	(9 <sup>-</sup> ) $\rightarrow$ (7 <sup>-</sup> )	75 (7)
678	1603	(10 <sup>-</sup> ) $\rightarrow$ (8 <sup>-</sup> )	29 (3)
684	1752	(10 <sup>-</sup> ) $\rightarrow$ (9 <sup>-</sup> )	12 (2)
724	1792	(11 <sup>-</sup> ) $\rightarrow$ (9 <sup>-</sup> )	36 (5)

TABLE IV: The energies ( $E_\gamma$ ) and relative intensities ( $I_\gamma$ ) of the  $\gamma$  rays assigned to  $^{143}\text{La}$  isotopes along with the spin and parity of the initial ( $J_i^\pi$ ) and the final ( $J_f^\pi$ ) states and the energy of the initial state ( $E_i$ ).

$E_\gamma$ (keV)	$E_i$ (keV)	$J_i^\pi \rightarrow J_f^\pi$	$I_\gamma$ (Err.)
93.9	1452.8	15/2 <sup>+</sup> $\rightarrow$ (13/2 <sup>-</sup> )	<16
(128.0)	1452.8	15/2 <sup>+</sup> $\rightarrow$ (13/2 <sup>+</sup> )	<15
133.4	424.7	(9/2 <sup>+</sup> ) $\rightarrow$ 7/2 <sup>+</sup>	50 (11)
156.0	1698.8	(17/2 <sup>+</sup> ) $\rightarrow$ (15/2 <sup>-</sup> )	2.8 (6)
170.5	2373.6	— $\rightarrow$ —	7 (2)
202.6	3830.9	— $\rightarrow$ (29/2 <sup>+</sup> )	<26
204.5	993.9	(13/2 <sup>+</sup> ) $\rightarrow$ 11/2 <sup>+</sup>	20 (4)
230.3	2373.6	(21/2 <sup>+</sup> ) $\rightarrow$ (19/2 <sup>+</sup> )	12 (2)
261.4	291.2	7/2 <sup>+</sup> $\rightarrow$ 3/2 <sup>+</sup>	194 (11)
291.2	291.2	7/2 <sup>+</sup> $\rightarrow$ 7/2 <sup>+</sup>	1000 (52)
302.5	2373.3	(21/2 <sup>+</sup> ) $\rightarrow$ (19/2 <sup>-</sup> )	43 (6)
325.7	1778.6	(17/2 <sup>+</sup> ) $\rightarrow$ 15/2 <sup>+</sup>	241 (24)
326.0	2798.3	(23/2 <sup>+</sup> ) $\rightarrow$ (21/2 <sup>-</sup> )	4 (1)
(326.0)	(3340.7)	— $\rightarrow$ (25/2 <sup>+</sup> )	<10
329.0	2472.3	(21/2 <sup>-</sup> ) $\rightarrow$ (19/2 <sup>+</sup> )	1.4 (3)
364.5	789.3	11/2 <sup>+</sup> $\rightarrow$ (9/2 <sup>+</sup> )	190 (16)
(364.7)	2143.2	(19/2 <sup>+</sup> ) $\rightarrow$ (17/2 <sup>+</sup> )	<5
371.8	2070.6	(19/2 <sup>-</sup> ) $\rightarrow$ (17/2 <sup>+</sup> )	75 (7)
394.8	1937.6	(17/2 <sup>-</sup> ) $\rightarrow$ (15/2 <sup>-</sup> )	25 (3)
404.7	1857.5	(17/2 <sup>-</sup> ) $\rightarrow$ 15/2 <sup>+</sup>	62 (6)
424.3	2203.1	— $\rightarrow$ (17/2 <sup>+</sup> )	17 (4)
424.7	424.7	(9/2 <sup>+</sup> ) $\rightarrow$ 7/2 <sup>+</sup>	1300 (130)
(424.8)	2798.3	(23/2 <sup>+</sup> ) $\rightarrow$ (21/2 <sup>+</sup> )	<8
435.0	2372.6	(21/2 <sup>-</sup> ) $\rightarrow$ (17/2 <sup>-</sup> )	6 (1)

453.8	1778.6	$(17/2^+) \rightarrow (13/2^+)$	92 (8)	614.9	2472.3	$(21/2^-) \rightarrow (17/2^-)$	18 (4)
458.7	1452.8	$15/2^+ \rightarrow (13/2^+)$	56 (5)	641.1	3014.7	$(25/2^+) \rightarrow (21/2^+)$	84 (9)
(489.0)	(2862.6)	— $\rightarrow (21/2^+)$	<26	655.1	2798.3	$(23/2^+) \rightarrow (19/2^+)$	23 (3)
498.1	789.3	$11/2^+ \rightarrow 7/2^+$	753 (60)	663.6	1452.8	$15/2^+ \rightarrow 11/2^+$	374 (21)
498.4	1857.5	$(17/2^-) \rightarrow (13/2^-)$	32 (2)	667.9	2738.5	$(23/2^-) \rightarrow (19/2^-)$	42 (6)
517.7	4348.6	— $\rightarrow$ —	26 (6)	674.6	2373.3	$(21/2^+) \rightarrow (17/2^+)$	12 (2)
527.8	2070.6	$(19/2^-) \rightarrow (15/2^-)$	26 (2)	690.4	2143.2	$(19/2^+) \rightarrow 15/2^+$	88 (9)
535.6	1324.9	$(13/2^+) \rightarrow 11/2^+$	156 (10)	704.9	1698.8	$(17/2^+) \rightarrow (13/2^+)$	178 (16)
548.9	1542.8	$(15/2^-) \rightarrow (13/2^+)$	115 (10)	724.1	3097.7	— $\rightarrow (21/2^+)$	30 (4)
569.2	993.9	$(13/2^+) \rightarrow (9/2^+)$	567 (49)	750.3	2203.1	— $\rightarrow 15/2^+$	22 (3)
569.8	1359.1	$(13/2^-) \rightarrow 11/2^+$	145 (10)	974.6	1763.9	— $\rightarrow 11/2^+$	13 (3)
595.0	2373.6	$(21/2^+) \rightarrow (17/2^+)$	194 (20)				
613.6	3628.3	$(29/2^+) \rightarrow (25/2^+)$	40 (10)				